ELSEVIER

A printed, recyclable, ultra-strong, and ultra-tough graphite structural material

Yubing Zhou [1,†], Chaoji Chen [1,†], Shuze Zhu [2,†], Chao Sui [3], Chao Wang [3], Yudi Kuang [1], Upamanyu Ray [2], Dapeng Liu [1], Alexandra Brozena [1], Ulrich H. Leiste [4], Nelson Quispe [2], Hua Guo [3], Azhar Vellore [5], Hugh A. Bruck [2], Ashlie Martini [5], Bob Foster [6], Jun Lou [3], Teng Li [2,*], Liangbing Hu [1,*]

[1] Department of Materials Science and Engineering, University of Maryland, College Park, MD 20742, United States
[2] Department of Mechanical Engineering, University of Maryland, College Park, MD 20742, United States
[3] Department of Materials Science and Nanoengineering, Rice University, Houston, TX 77005, United States
[4] Department of Aerospace Engineering, University of Maryland, College Park, MD 20742, United States
[5] Department of Mechanical Engineering, University of California Merced, Merced, CA 95343, United States
[6] Trinity Industries, Inc., Dallas, TX 75207, United States

The high mechanical performance of common structural materials (e.g., metals, alloys, and ceramics) originates from strong primary bonds (i.e., metallic, covalent, ionic) between constituent atoms. However, the large formation energy of primary bonds requires high temperatures in order to process these materials, resulting in significant manufacturing costs and a substantial environmental footprint. Herein, we report a strategy to leverage secondary bonds (e.g., hydrogen bonds) to produce a high-performance and low-cost material that outperforms most existing structural compounds. By dispersing graphite flakes and nanofibrillated cellulose (NFC) in water at room temperature to form a stable and homogeneous solution with a high solid concentration (20 wt%), we demonstrate this slurry can be scalably printed to manufacture a graphite-NFC composite that exhibits a high tensile strength (up to 1.0 GPa) and toughness (up to 30.0 MJ/m^3). The low density of graphite and cellulose leads to a specific strength of the composite (794 MPa/(g cm^{-3})) that is significantly greater than most engineering materials (e.g., steels, aluminum, and titanium alloys). We demonstrate how hydrogen bonds between the graphite flakes and NFC play a pivotal role in the superb mechanical performance of the composite, also enabling this low-cost material to be recyclable for an environmentally sustainable solution to high performance structural materials.

Introduction

A widely used strategy in the design of structural materials featuring high mechanical performance is to leverage strong primary bonds between constituent atoms [1–4]. For example, the carbon–carbon covalent bonds that make up carbon fibers result in a tensile strength of up to 4 GPa [5]; strong metallic bonds lead to the high melting points of metals; and the high stiffness and hardness of ceramics are dictated by strong ionic bonds. The high formation energy of primary bonds enables these kinds of desirable mechanical properties, however, it also requires the use of high processing temperatures and significant energy consumption during manufacture. As a result, the high performance of structural materials often comes at a price of adverse environ-

* Corresponding authors.
E-mail addresses: Li, T. (lit@umd.edu), Hu, L. (binghu@umd.edu).
† These authors contributed equally to this work.

1369-7021/ https://doi.org/10.1016/j.mattod.2019.03.016

mental impact. Furthermore, while the energy barrier required to break a primary bond is high, once broken, it is also difficult to recover, which can result in undesirable material properties, such as the mutual conflict between strength and toughness (i.e., stronger materials are often brittle, such as ceramics) [6].

Secondary bonds (e.g., hydrogen bonds) have modest bonding energy, but can readily form between atoms or functional groups [7]. For example, a hydrogen bond can easily form when two hydroxyl groups come within proximity of each other. When such a hydrogen bond is broken (e.g., by separating the two hydroxyl groups apart), new hydrogen bonds can easily reform after the hydroxyl groups move to the vicinity of other neighboring hydroxyl groups. This unique feature of secondary bonds inspires the material design strategy to achieve highly desirable material properties. For example, cellulose nanopaper made of densely packed nanofibrillated cellulose (NFC) can be made orders of magnitude stronger and tougher than regular paper made of cellulose microfibers due to the significantly increased number of hydrogen bonds between the rich hydroxyl groups along neighboring cellulose molecular chains [8].

Herein, we demonstrate a material design strategy that utilizes secondary bonding to achieve a high performance structural material at low cost and with a significantly reduced environmental footprint. Using a room temperature, scalable, and surfactant-free process, we show how few-layer, highly crystalline graphite flakes can be directly exfoliated from commercial graphite powder in an aqueous solution using NFC as the dispersing agent. The resulting graphite-NFC slurry can then be printed in large area and cast-dried into an ultra-strong and ultra-tough composite that outperforms most metals and alloys.

Results and discussion

NFC contains both hydrophilic functional groups and hydrophobic C–H moieties [9]. The hydrophobic sites interact with the hydrophobic plane of the graphite flakes while the hydrophilic hydroxyl groups form hydrogen bonds with the defective edges, enabling NFC to directly exfoliate graphite as a dispersant in a manner similar to surfactant aided graphite dispersion and exfoliation [10–12]. The presence of adsorbed NFC fibers on the surface prevents the re-stacking of graphite flakes due to the electrostatic repulsive forces generated by the charged NFC carboxyl groups (Figs. 1a,b, S1). Transmission electron microscopy (TEM) and selected area electron diffraction (SAED) of the resulting composite reveal the exfoliation of the bulk graphite into few-layer graphite flakes, which are structurally uniform, with high crystal quality that is well-preserved during the secondary bond formation process (Fig. S2). Note that the strong inclination of few-layer graphite flakes to undergo π-π stacking always occurs during conventional exfoliation in a solvent-dispersed system, leading to limited dispersion stability, thus requiring vast amounts of solvent (1000-times relative to the weight of the solid) to achieve a homogeneous and stable dispersion [13–16]. However, in our system, the NFC dispersal process results in an aqueous flowable slurry with a significant high solid content of up to 20 wt% (Figs. 1c, S3a,b). Surprisingly, the viscosity of the 20 wt% graphite-NFC slurry (i.e. 10 wt% NFC) is as low as that of the 4 wt% pure NFC samples (Fig. S3c,d), which is an excellent feature for printing. With water evaporation, the graphite-NFC slurry can be further concentrated up to 30 wt% but retains fluid-like behavior (Fig. S4). This highly concentrated graphite slurry paves the way for the effective fabrication of graphite-based materials.

The graphite-NFC composite is low-cost, as the source materials for the graphite flakes and NFC (raw graphite and wood chips, respectively) are earth abundant and inexpensive (Fig. 2a). NFC can be prepared using a top-down approach from wood cell walls (Fig. S5a). Graphite flakes can then be dispersed at room temperature by NFC in an aqueous solution with no need for a surfactant. Such a process is readily scalable to produce the graphite-NFC slurry in large quantities (Figs. 2b, S5b,c). The slurry of few-layer graphite flakes exfoliated in the NFC suspension is relatively stable due to the existence of charged hydroxyl and carboxyl groups (Zeta potential = −53.9 mV, pH = 7; Fig. S1c), as no clear sedimentation is observed even after six months (Fig. S5c,d).

The slurry nature of the graphite-NFC solution also enables the scalable manufacture of the resulting composite via a printing process. As water evaporates from the solution, the mobility of the graphite flakes is strongly limited by hydrogen bonding with the surrounding NFC network, leading to a dense layer of the solid composite (Figs. 2c, S6) that can be easily peeled off from the glass substrate (Fig. S7). In this manner, a graphite-NFC composite layer 120 cm × 30 cm × 22 μm in size can be readily manufactured (Fig. 2d). Due to the laminated structure of the graphite-NFC composite (Fig. 2e,f), the material is highly flexible and can be readily bent into a small radius (~2 mm) without breaking (Fig. S8). The random distribution of constituent graphite flakes in the plane of the composite dictates its isotropic in-plane mechanical properties (Fig. 2g), as evident from the circular small angle X-ray scattering (SAXS) pattern perpendicular to the plane (Fig. 2h). The graphite flakes are also highly aligned in parallel to the plane of the composite, as evident from the anisotropic SAXS pattern from the direction parallel to the plane (Fig. 2h).

The graphite-NFC composite exhibits an array of exceptional behaviors that are highly desirable for structural materials but generally difficult to achieve. Fig. 3a compares the key mechanical properties (specific strength and toughness), processability, cost, and recyclability of the graphite-NFC with those of representative structural (e.g., steel, aluminum alloy, polymer composites) and high-performance engineering materials (e.g., carbon fiber and cellulose nanopaper). When it comes to material choice, particularly for structural applications, density is a major consideration. Metallic alloys are some of the strongest and toughest engineered materials produced, but their high density limits their practical use when being lightweight is vital for energy efficiency. The graphite-NFC composite exhibits the unprecedented integration of high mechanical properties, low density, and low cost that exceeds the most widely used structural materials, including steel, aluminum alloy, NFC nanopaper, polyethylene composites, and even carbon fibers [20–22].

Fig. 3b shows the typical tensile stress–strain curves of the graphite-NFC composite, cellulose nanopaper, and graphite after hot press (see Methods for details), respectively. The ultimate tensile strength and work of fracture obtained from the

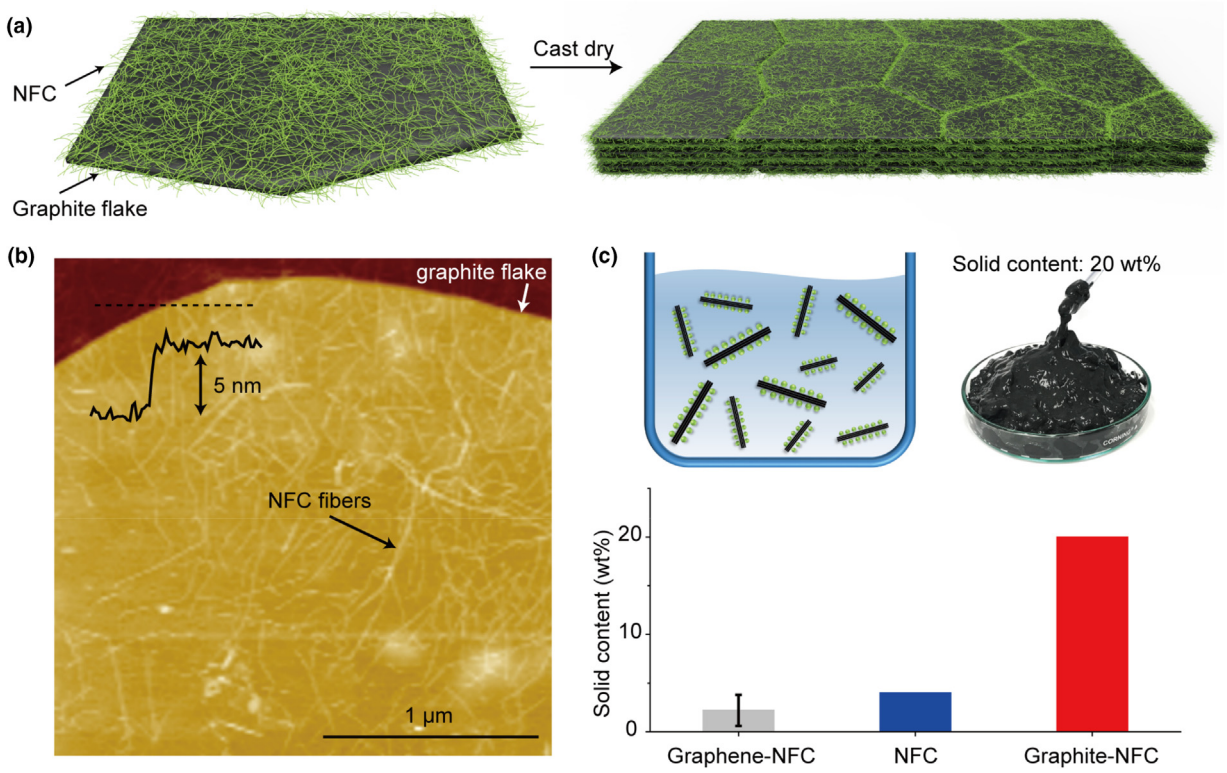

FIGURE 1

NFC-enabled dispersion of graphite with a high solid content of 20 wt%. (a) Schematic representation of how NFC nanofibers attach to and disperse graphite flakes through the interaction between the materials' hydrophobic sites as well as hydrogen bonding between the NFC hydroxyl groups and the defective edges of the graphite flakes. After cast-drying, the resulting composite is composed of NFC fibers and multilayered graphite flakes. (b) AFM image of a graphite flake exfoliated by NFC. The NFC fibers are closely associated with the surface of the graphite flake. (c) The solid content of the resulting graphite-NFC slurry (1:1 mass ratio) is shown to be 4∼5 times higher than that of typical NFC and reported graphene-NFC solutions [17–19].

stress–strain curves show that optimal performance can be achieved when multilayer graphite flakes hybridize with NFC (Fig. 3d,e). As graphite flakes are hybridized into the NFC matrix, the ultimate tensile strength increases by ∼ 3.7-times, from 245 ± 47 MPa (NFC) to 901 ± 129 MPa (graphite-NFC composite), and the work of fracture increases nearly 5.9-times from 4.7 ± 0.8 MJ/m^3 (NFC) to 27.7 ± 2.3 MJ/m^3 (graphite-NFC composite). Unlike traditional structural materials, the graphite-NFC composite demonstrates both substantially enhanced ultimate tensile strength and the work of fracture (Fig. 3c). The specific tensile strength of our graphite-NFC composite is even higher than ultrastrong low-density steel and titanium alloys (Fig. 3f) [23,24]. Observations of the fracture surface after tensile failure between multilayer graphite flakes reveal the presence of NFC mimicking the organic layer in nacre with a "brick-and-mortar" microstructure, in which the initially random network of constituent nanofibers aligns along the tensile loading direction (Fig. S9).

The facile formation and re-formation of hydrogen bonds between the graphite flakes and NFC also endow the graphite-NFC composite with good recyclability. The graphite-NFC composite can be dispersed in water to reconstruct a stable and uniform slurry with the same properties as the original slurry and re-form a composite via cast-drying (Fig. S10). It is noteworthy that the competition between recyclability and stability against water is a long-standing issue for cellulose-based materials. Balance is needed between the two distinct properties for practical applications. Our experimental results show that the stability of the graphite-NFC composite against humidity/water can be improved substantially by surface coating as demonstrated by both the stable dimensions and mechanical properties of the material post-treatment (Fig. S11).

Our bottom-up processing approach provides the ability to fabricate graphite-NFC block materials by hot pressing multiple layers of the graphite-NFC composite (inset in Fig. 3f, Fig. S12). We performed ballistic tests on NFC nanopaper, a commercial graphite plate, and the graphite-NFC composite block (1 mm thick), in which the ballistic energy absorption of the samples is defined by the kinetic energy loss after a cylindrical steel projectile perforates the sample. When the same ballistic test is conducted using these three kinds of materials, the resulting energy absorption per unit thickness of the block graphite-NFC material was 6.13 ± 0.16 KJ/m, a remarkable 4.6- and 5.4-times increase from that of NFC nanopaper and the commercial graphite plate, respectively (Fig. 3g). The graphite flakes, with some parts still embedded in the NFC matrix, break along the incident direction of the projectile, indicating substantial energy dissipation during the projectile perforation (Fig. 3h). In addition, the scratch hardness of the graphite-NFC composite (310 MPa) was 1.5-times higher than that of the NFC nanopaper (200 MPa) (Fig. S13). The fracture toughness also increased by 7.8-times (Fig. S14).

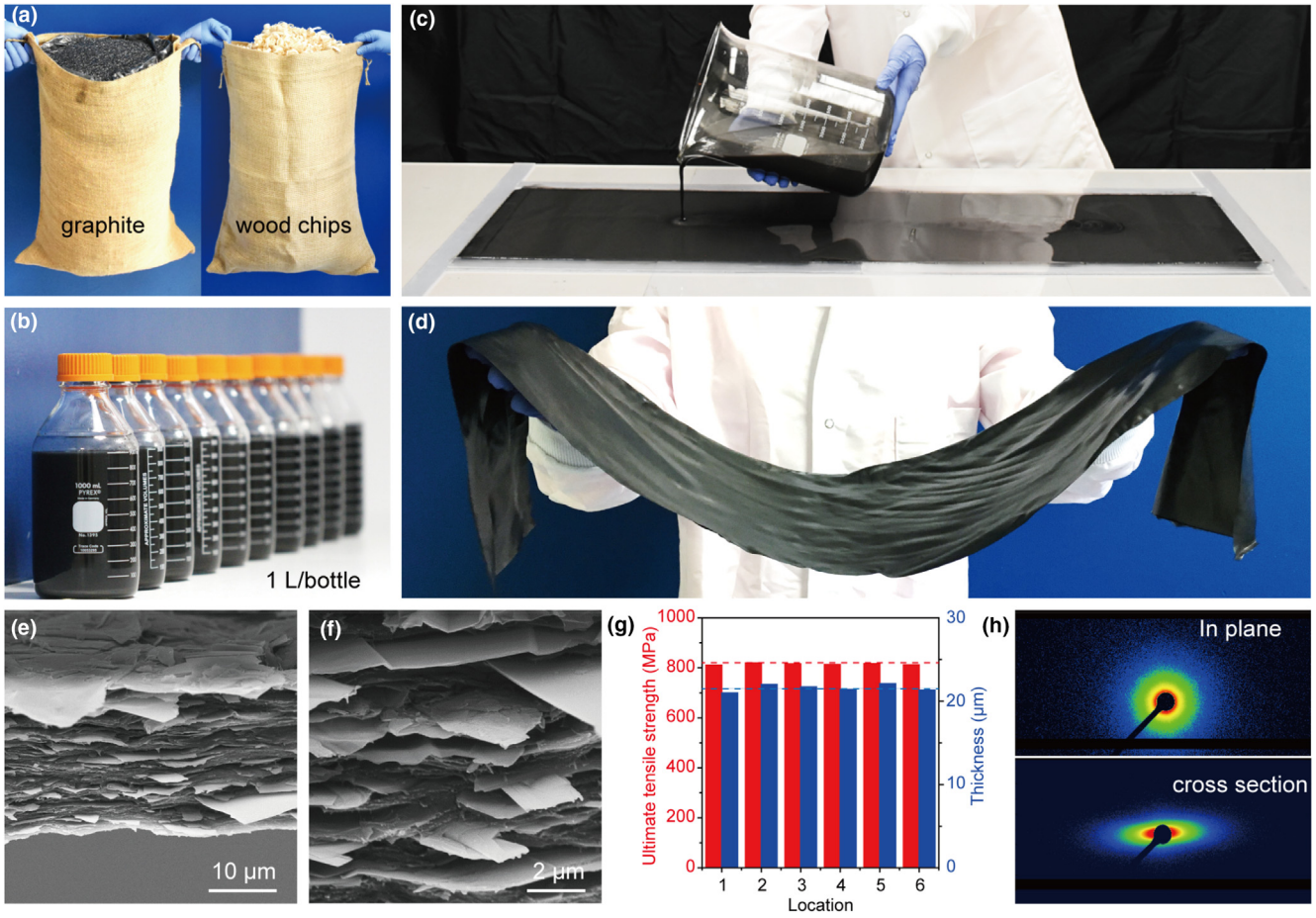

FIGURE 2

Production of the NFC-enabled dispersed graphite slurry and the hybrid composite (1:1 mass ratio). (a) Large-volumes of graphite and wood chips. NFC is obtained from wood chips. Graphite is dispersed and exfoliated in NFC suspensions under sonication. (b) Large-volume graphite-NFC slurries produced by sonication. (c) Images of the fabrication process of the graphite-NFC composite, and (d) a large scale (120 cm × 30 cm) graphite-NFC composite sheet. (e, f) Cross-sectional-view SEM images of the graphite-NFC composite. (g) The homogeneous thickness and ultimate tensile strength obtained from different locations of the large-sized graphite-NFC composite. (h) SAXS patterns of the graphite-NFC composite in the plane (top) of the material and along the cross-section (bottom).

Molecular dynamics simulations provide a mechanistic explanation for the observed mechanical properties of the graphite-NFC composite (1:1 mass ratio), in which the strong interactions between the graphite flakes and NFC fibers play a pivotal role in the high strength and toughness. The hydrophilic behavior of NFC is attributed to the hydroxyl groups that are located on the surface of the NFC fibers. The exposure of the hydrophobic C–H bonds also causes hydrophobic faces to form in the elementary fibers, which enable hydrophobic interactions with the hydrophobic plane of the graphite (Figs. 4a,d,g, S15). Meanwhile, the spatial gaps between the edges of the graphite flakes are filled with the flexible NFCs (Fig. 4a-f). A large amount of the interfaces between the graphite flake edges and NFC matrix are thus hydrogen bonded, which significantly enhances load transferring between graphite flakes. Due to the presence of the graphite hydrophobic surfaces, the hydrogen bonding networks projected along the tensile direction are densified (Fig. S15), thus the load transferring capacity of the NFC matrix also increases (Fig. 4h,i). The synergistic interaction between the graphite flakes and NFC substantially increases the load resistance of the composite to failure (i.e., high strength) and the energy dissipation during composite failure (i.e., high toughness). In contrast, in a pure graphite film there are only a limited number of hydrogen bonding sites at the flake edges, and the inter-flake interactions are essentially weak van der Waals forces (Fig. 4c,f). As a result, pure graphite is weak and brittle.

The high quality of graphite flakes also plays a pivotal role in the superb mechanical performance of the graphite-NFC composite. In previous studies, various one dimensional (1D) and two dimensional (2D) nanomaterials have been hybridized to produce high-performance structural materials [19,25]. Prior to the hybridizing process, graphite as the starting material was usually treated vigorously with harsh chemicals to obtain graphene, GO, or RGO, which is neither environmentally friendly, nor cost-effective [26–28]. To achieve 2D materials with nanometer thickness (graphene, graphene oxide, etc.), intensive mechanical energy or/and harsh chemicals were used during fabrication, resulting in highly defective 2D structures with severely reduced lateral size (~1 μm) [17,18]. In contrast, our process only involves mild mechanical sonification without any harsh chemicals or

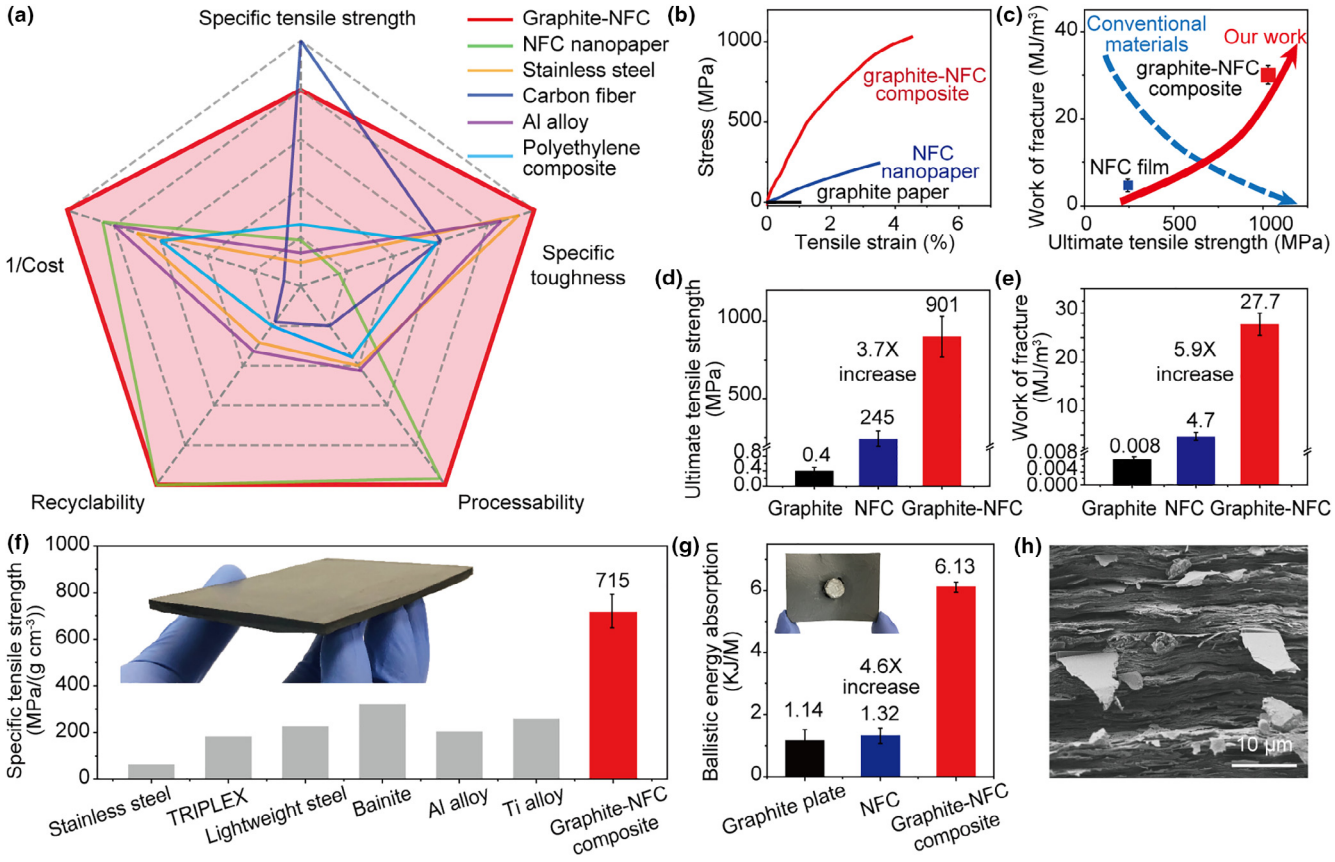

FIGURE 3

Superb mechanical performance of the graphite-NFC composite (1:1 mass ratio). (a) A radar plot showing a comparison among graphite-NFC composites, NFC nanopaper, stainless steel, carbon fiber, Al alloy, and polyethylene composite. The results are normalized by the maximum value of each mechanical characteristic. (b) Stress–strain curves of graphite-NFC, NFC nanopaper, and graphite paper. (c) The graphite-NFC composite is both substantially stronger and tougher than NFC nanopaper, defeating the conventional conflict between strength and toughness. (d, e) Comparison of the ultimate tensile strength (d) and work of fracture (e) of the graphite-NFC composite, NFC nanopaper, and graphite paper, respectively. (f) Specific tensile strength of the graphite-NFC composite compared with strong metallic alloys. (g) The ballistic energy absorption of the NFC, commercial graphite plate and graphite-NFC composite. Inset: Photo of the graphite-NFC composite after the ballistic test. (h) Cross-sectional SEM image of the vertically stacked multilayer graphite-NFC composite after the ballistic test.

surfactants, leading to high-quality graphite flakes with large lateral size (11 ± 3.3 μm) and low thickness (mostly 3–5 layers of graphene) (Fig. S16). Consequently, the resulting graphite-NFC composite can achieve strength and toughness significantly higher (by up to 5-times) than those composites reported previously with a potentially much lower cost. Table S1 summarizes the detailed comparison of material building blocks, process conditions, manufacturability, and mechanical performance of the resulting materials in prior studies and the present study [17,18,29–34].

We further validated the strengthening and toughening mechanisms emerging from the molecular dynamics simulations by *in situ* atomic force microscopy (AFM) pulling tests, which revealed the deformation and failure characteristics of the graphite-NFC composite. At the cross-section of the graphite-NFC composite, a protruding graphite flake was first glued to the AFM tip. The AFM tip was then moved apart from the cross-section, applying a tensile load to the graphite flake until failure occured. Among the five graphite flakes tested, four failed by cohesion fracture of the flake, while one failed by pulling the flake out of the composite (Figs. 5a-h, S17a-k). Among the four cohesion fracture cases, one case involved full fracture of the flake while the other three cases resulted in partial fracture (see Figs. 5a-d,i,j, S17f or details). The partial fracture was mainly attributed to the uneven edges of the multi-layer graphite flakes, which makes it difficult to ensure that each layer of the graphite flakes are strongly bonded to the AFM probe. Therefore only the graphite layers bearing loading can be stretched and other layers were well-preserved. The fracture strength (σ_f) of the graphite flakes can be estimated by $\sigma_f = F_{max}/nt_0w_f$, in which F_{max} is the pulling force at the occurrence of flake fracture, n is the fractured layer number, w_f is the effective fracture width near the fracture surface, and $t_0 = 0.34$ nm (i.e., the inter-layer thickness of graphite). The w_f can be directly measured from the scanning electron microscopy (SEM) images, however, it is difficult to measure n accurately. Therefore, the fracture strength (σ_f) as a function of flake layer number (n) is plotted in Fig. 5h based on the AFM test results (Table S2). For example, for $n = 4$, the corresponding fracture strength in the four tests ranges from 0.72 GPa to 0.94 GPa, with an average of 0.83 GPa, which is in reasonable agreement with the tensile test measurements (Fig. 3b). The full or partial fracture of the graphite flakes in AFM tests also

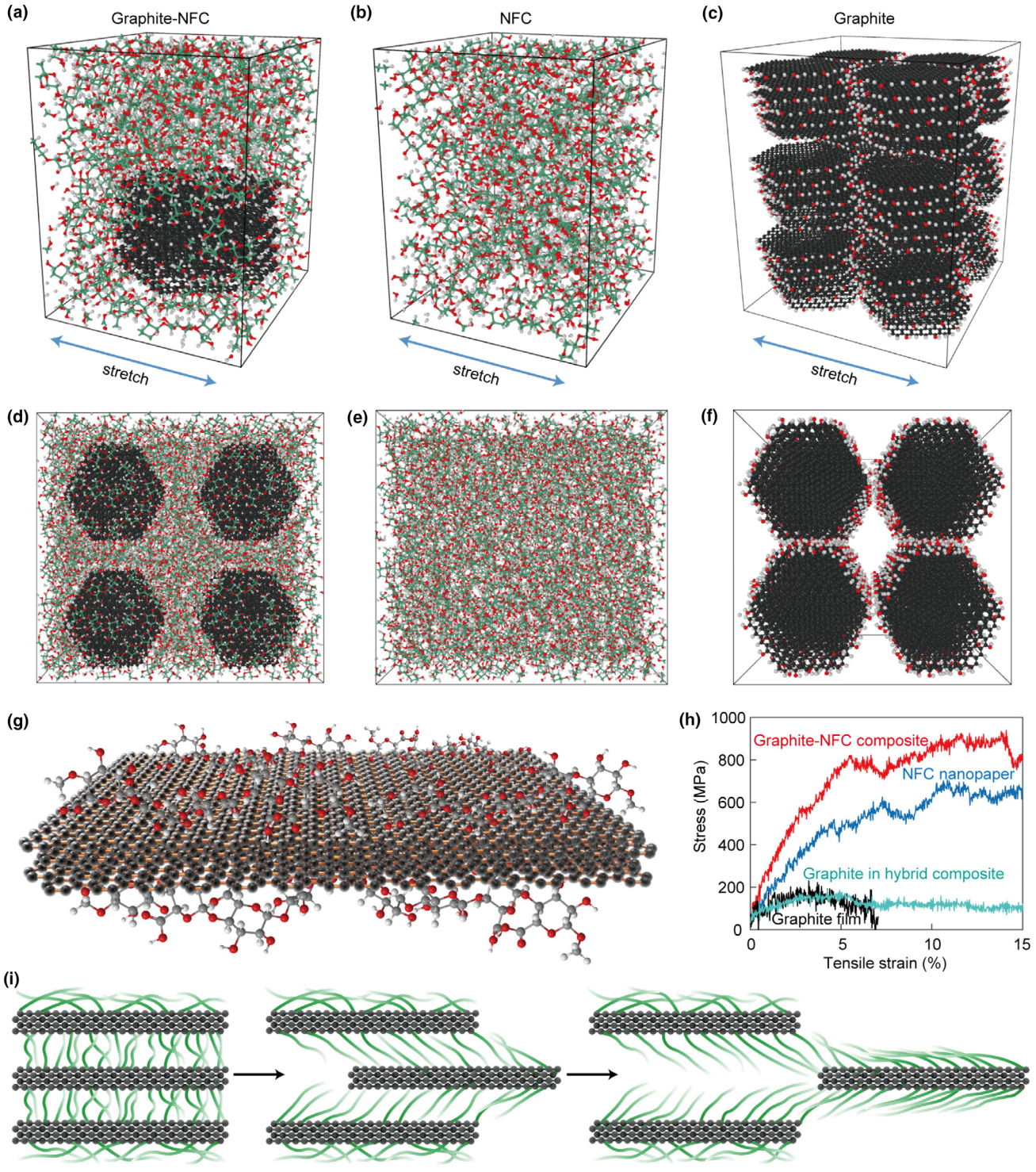

FIGURE 4

(a–c) Structures of the graphite-NFC hybrid before enforcing deformation (a). Structures of the pure NFC before enforcing deformation (b). Structures of the pure graphite before enforcing deformation (c). The bounding box denotes the periodic boundary. Arrows denote the tensile loading. (d–f) Perspective views showing how the NFC matrix could help connect the graphite stacks by filling up the spatial gaps. Bounding boxes denote periodical boundaries. These presentations contain periodic images of the simulation cell for better clarity. Real graphite stacks would have a more complicated and irregular shape. (g) Schematic to show how NFC attaches to the graphite flakes through the interaction between its hydrophobic sites and the hydrophobic plane of the graphite, as well as hydrogen bonding between the NFC hydroxyl groups and the defective edges of the graphite flakes. (h) Engineering stress–strain curves for three structures from molecular dynamics simulations, including the graphite-NFC composite (red), pure NFC (blue), and pure graphite (black). Also plotted in cyan is the contribution of the graphite stack in the graphite-NFC hybrid model to the overall stress–strain curve, which demonstrates that the mechanically rigid graphite stacks are an active load-bearing agent in the graphite-NFC composite that renders its high strength and toughness. (i) Schematic to show the fracture process of the graphite-NFC composite under tension.

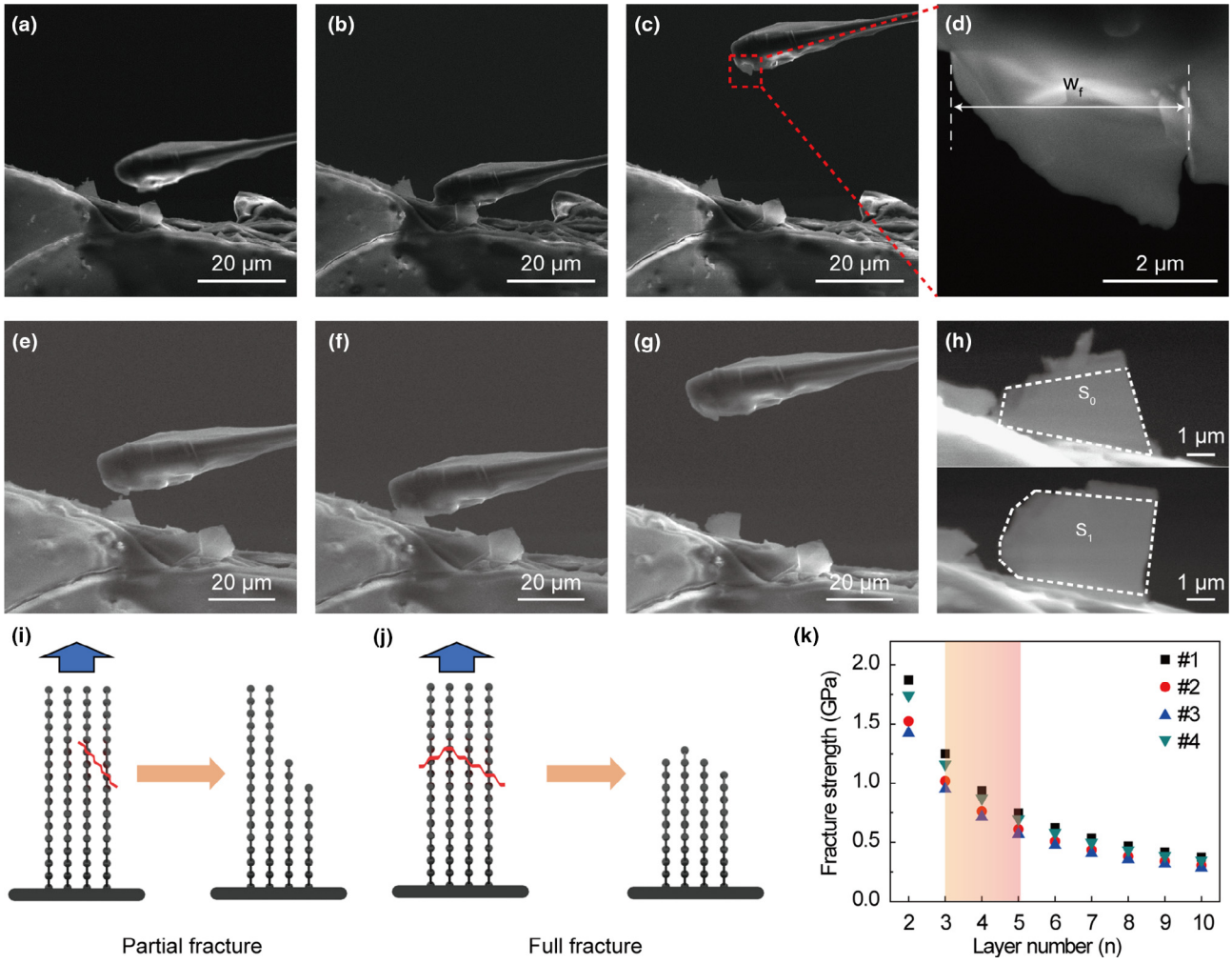

FIGURE 5

(a-h) *In situ* AFM pulling test of one individual graphite flake from the NFC matrix. (b, f) The AFM probe is parallel to the fracture surface of the graphite-NFC composite and attached to the edge of a single graphite flake. (c, g) The AFM probe was moved away from the fracture surface until a potential failure occurs. (d, h) Magnified image to show that the graphite flake was partially fractured. (i, j) Schematic of fracture failure, including (i) full fracture and (j) partial fracture. (k) Estimated fracture strength as a function of the layer number of the graphite flake. The shaded area corresponds to the range of the typical layer number of the graphite flakes in this work.

suggests strong bonding between graphite flakes and NFC in the composite (otherwise, the graphite layers that are glued to the AFM probe can easily slide off from the flake given the weak interlayer interactions in pure graphite). This offers further support for the underlying strengthening and toughening mechanisms revealed by the mechanics simulations.

Conclusion

In summary, a secondary bonding strategy was developed to produce a mechanically robust graphite-NFC composite via a room-temperature, scalable, and surfactant-free solution process. Commercial graphite powders can be directly exfoliated into few-layer graphite flakes by the aqueous solution of native NFC, forming an ultra-high concentrated (20 wt%) and stable graphite-NFC dispersion. A large-scale (120 cm × 30 cm) graphite-NFC composite with a laminated structure can be achieved through an industrially mature cast-drying process. NFC acts not only as an effective aqueous dispersion agent, but also as a "glue" to tightly stick the multilayer graphite flakes together through secondary bonds, including hydrophobic interactions and hydrogen bonding. Remarkably, both a record-high mechanical tensile strength (up to 1.0 GPa) and toughness (up to 30.0 MJ/m^3) were simultaneously achieved in the resulting graphite-NFC composite. Being lightweight, the graphite-NFC composite surpasses most conventional primary bond-based structural materials in terms of specific strength and toughness, including various steels, alloys, and even some carbon fibers. The fabrication of this composite requires relatively little energy without producing harmful waste, making it a scalable, economically feasible, environmentally friendly, and recyclable material, thus opening new opportunities for developing high-performance structural materials in a more sustainable manner.

Materials and methods

Preparation of graphite-NFC composites

Commercial graphite powder (Asbury Carbons 3061) and 2 wt% NFC solution were mixed together with a solid mass ratio of 1:1 for graphite to NFC. All the samples have a graphite to NFC mass

ratio of 1:1. The dispersion process was performed using a Vibra-Cell ultrasonic liquid processor for 5 min, and then bath sonicated for 15 min (FS110D, Fisher Scientific). After sonication, the graphite flakes were well dispersed in the NFC solution. The obtained graphite-NFC slurry was degassed for 20 min in a vacuum pumping system until no bubbles were observed in the slurry. The graphite-NFC slurry can be concentrated by placing it on a heating stage at 110 °C with high speed stirring to ensure the uniformity of the whole system. The graphite-NFC composites were prepared by cast-drying the 20 wt% slurry. The final composite with 20 to 50-μm thickness and ~1.2 g/cm^3 density was obtained after a 60 °C hot press for 24 h.

For control experiments, we prepared NFC films using a similar procedure except without the addition of graphite. The graphite film was also prepared using a similar procedure except that the graphite solution was intensively washed by $ZnCl_2$ and water to remove NFC before pressing. All the NFC nanopapers and graphite-NFC composites used for mechanical testing were pressed at 60 °C under a force of about 50 kN for 24 h using a hot press (YLJ-HP88V-250, MTI). The size of pressed samples are generally 10 cm × 10 cm, so the applied pressure is can be up to 5 MPa. The NFC nanopapers and graphite-NFC composites were hot pressed before completely dry in order to be full densified. The applied pressure increased gradually, and usually reached 50 kN in 4 h, then kept at 50 kN for 20 h. For the graphite-NFC composites without hot press, the ultimate tensile strength is 430 ± 19 MPa.

To fabricate block materials from the single graphite-NFC composites sheet, the single sheet should not be completely dried at first. Then multiple sheets are stacked together in the hot press at 60 °C under a force of about 50 kN for 48 h.

Characterizations

SEM images were taken with a Hitachi SU-70 Schottky field emission gun scanning electron microscope (2–5 kV, depending on the sample state). All samples were coated by gold sputtering for 90 s prior to observation. TEM and high resolution TEM studies were carried out using a field-emission-gun JEOL-2100F microscope, operated at 200 kV and equipped with a Gatan Tridiem 863 GIF (Gatan Imaging Filter) system. All the high-resolution TEM images were recorded under the Scherzer defocus condition. The thickness of the graphite flakes was measured by the number of layers in the high resolution TEM images (more than 50 images) to obtain the statistical distribution. AFM (Digital Instrument Nanoscope V) was applied to characterize the morphology of the NFC-coated graphite flakes in tapping mode. The lateral size of the graphite flakes was characterized by optical microscopy (OM, STM6-Olympus Measuring Microscopes). SAXS measurements were made using a Xenocs Xeuss SAXS/WAXS/GISAXS small angle X-ray scattering system with an X-ray wavelength of $\lambda = 0.957$ Å and sample-to-detector distance of 8.422 mm. The beam size was 24 × 11 mm (horizontal × vertical), and the scattering patterns were recorded using a single-photon counting detector (Pilatus 1 M, Dectris) with a pixel size of 172 × 172 μm^2. The rheological properties of the slurries were investigated using a Discovery Hybrid HR-2 rheometer (TA instruments) with a peltier plate fixture of 25-mm disposable parallel plates. The Zeta potential was determined using a Zetasizer Nano ZS90.

Tensile tests

A single column tabletop model testing systems (Instron, USA) was used to perform mechanical tests. A 1000 N load cell was used with a nominal strain rate of 0.5 mm/min, because of its optimal data range. At least 5 specimens were measured from each sample. All the samples for mechanical testing were cut into rectangular strips with a width of 2 mm and lengths of 30 mm by a razor blade. To exclude the influences of humidity on mechanical properties, all samples were kept in a constant humidity environment (50%) for one day before tensile tests, and all tensile tests were performed under an identical environment in ambient conditions.

Stability test against moisture

Two graphite-NFC composites with dimensions of approximately 30 mm length by 15 mm width by 3.5 mm thickness were prepared. Following a painting method widely used in industry, we coated one graphite-NFC composite with a thin layer of oil-based paint (Polyurethane, Minwax). After the paint was totally dry, the samples with and without paint coating were put into the humidity chamber (LHS-150HC-II, set to 25 °C, 98% RH) and measured at regular intervals. The dimensions of the samples after various intervals in the humidity chamber were recorded.

Fracture toughness test

We tested the fracture toughness using a method developed by Rivlin and Thomas. A more detailed description is provided in Ref. [8]. In brief, samples with a rectangular shape were prepared to be loaded between the clamps of the mechanical test machine. A precrack is introduced along the mid-line of the sample between the two clamps (e.g., inset in Fig. S14a). The samples are positioned such that both the length of the sample and the length of the precrack are much larger than the initial separation between the two clamps. During the increase of the separation between the two clamps, the precrack will turn into a propagating crack. At this moment, we record the final separation between the two clamps. We then also loaded a sample without precrack beyond the recorded final clamp separation. To calculate the fracture toughness, we first calculated the work done by the applied load as the area beneath the load–displacement curve of the sample without precrack within the range from the initial clamp separation (zero displacement) to the recorded final clamp separation. Then the fracture toughness is calculated as the work (calculated above) divided by the product of the length and the thickness of the sample.

Ballistic tests

We used a gas gun to conduct ballistic tests on the graphite-NFC composites. The entire gas gun setup was comprised of pressure indicator frames (PIM), two cylinders filled with compressed nitrogen (N_2), a pressure chamber 127 mm in diameter, a barrel-length of 190.5 mm, a nozzle of 1156 mm in length and an internal diameter of 12.5 mm. The PIM has adjustable dials for controlling the pressure inside the N_2 cylinders. Using those

dials, one cylinder was used to pressurize the barrel chamber and another was used to control the firing valve pressure. Just after the projectile is fired, the pressure inside the cylinder force opens the valve and drives the projectile motion. The accelerated projectile then travels through the whole barrel-length to strike the sample, fastened by clamps in a suitable designed holder, and perforating it. In the tests, the projectile used was cylindrical and made of stainless steel with a diameter of 11.85 mm, length of 51.77 mm, and mass of 0.046 kg. The chamber pressure was set to ~2.21 MPa. The whole process was captured by two high-definition Phantom v12 digital cameras, which were controlled by the Phantom Camera Control software. The software helps us to post-process the videos of the projectile before and after perforating the sample and thereby calculating the initial and final velocities. Subsequently, we evaluate the ballistic energy absorption of the test sample by calculating the kinetic energy loss that occurs due to the cylindrical steel projectile perforating the sample.

Scratch hardness tests

The scratch resistance of the graphite-NFC composite was evaluated according to the Standard Test Method for Scratch Hardness, ASTM G171-03(2009) using a linear reciprocating tribometer (Rtec Instruments Multi-Function Tribometer). The test was performed by applying a normal load on a diamond spheroconical tip indenter and moving the tip laterally at a constant speed. Each scratch hardness value was determined as an arithmetic mean of a set of three scratches made side by side at different locations.

Acknowledgments

We acknowledge the support of the Maryland Nanocenter, its Surface Analysis Center, and the AIMLab. We acknowledge the Dynamic Effects Lab under William L. Fourney in the Mechanical Engineering department at the University of Maryland for conducting the ballistic tests using their air-gun ballistic tester. The authors acknowledge the University of Maryland supercomputing resources (http://hpcc.umd.edu) made available for conducting the research reported in this work. The in situ AFM pulling test efforts were supported by the U.S. Department of Energy, Office of Basic Energy Sciences under Grant number DE-SC0018193.

Author contributions

Y. Zhou, C. Chen, and S. Zhu contributed equally to this work. L. Hu and Y. Zhou contributed to the idea and experimental design. Y. Zhou and D. Liu contributed to the graphite slurry preparation and the film formation. Y. Zhou and C. Chen contributed to the mechanical measurements. U. Ray, N. Quispe, U. Leiste, H. Bruck, and T. Li contributed to the mechanical tensile and ballistic tests. C. Sui, C. Wang, H. Guo and J. Lou contributed to *in situ* AFM pulling tests. Y. Kuang contributed to the 3D illustrations. Y. Zhou and C. Chen contributed to the characterization *via* SEM and TEM. A. Vellore and A. Martini contributed to the indentation and scratch hardness tests. S. Zhu and T. Li contributed to both mechanical simulations and analysis. L. Hu, Y. Zhou, T. Li, C. Chen, and A. Brozena contributed to writing the paper. All authors contributed to commenting on the final manuscript.

Appendix A. Supplementary data

Supplementary data to this article can be found online at https://doi.org/10.1016/j.mattod.2019.03.016.

References

[1] K. Lu et al., Science 324 (5925) (2009) 349.
[2] L.-B. Mao et al., Science 354 (6308) (2016) 107.
[3] P. Podsiadlo et al., Science 318 (5847) (2007) 80.
[4] G. Wu et al., Nature 545 (7652) (2017) 80.
[5] X. Zhang et al., Adv. Mater. 19 (23) (2007) 4198.
[6] Y. Wei et al., Nat. Commun. 5 (2014) 3580.
[7] R.P. Sijbesma et al., Science 278 (5343) (1997) 1601.
[8] H. Zhu et al., Proc. Natl. Acad. Sci. 112 (29) (2015) 8971.
[9] Y. Habibi et al., Chem. Rev. 110 (6) (2010) 3479.
[10] Y. Hernandez et al., Nat. Nanotechnol. 3 (9) (2008) 563.
[11] M. Lotya et al., J. Am. Chem. Soc. 131 (10) (2009) 3611.
[12] R.J. Smith et al., Adv. Mater. 23 (34) (2011) 3944.
[13] D. Li et al., Nat. Nanotechnol. 3 (2) (2008) 101.
[14] K.R. Paton et al., Nat. Mater. 13 (6) (2014) 624.
[15] G. Eda et al., Nat. Nanotechnol. 3 (5) (2008) 270.
[16] L. Niu et al., Small 12 (3) (2016) 272.
[17] D. Han et al., Carbohydr. Polym. 83 (2) (2011) 966.
[18] N.D. Luong et al., J. Mater. Chem. 21 (36) (2011) 13991.
[19] P. Laaksonen et al., Angew. Chem. 123 (37) (2011) 8847.
[20] H. Ku et al., Compos. B Eng. 42 (4) (2011) 856.
[21] C. Sauder et al., Carbon 42 (4) (2004) 715.
[22] T. Dursun, C. Soutis, Mater. Des. (1980–2015) 56 (2014) 862.
[23] S.-H. Kim et al., Nature 518 (7537) (2015) 77.
[24] F. Gil et al., Mater. Sci. Eng., A 349 (1–2) (2003) 150.
[25] Q. Cheng et al., ACS Nano 9 (3) (2015) 2231.
[26] L. Dong et al., Chem. Mater. 29 (2) (2017) 564.
[27] L. Dong et al., Chem. Soc. Rev. 46 (23) (2017) 7306.
[28] K.P. Loh et al., Nat. Chem. 2 (12) (2010) 1015.
[29] C.-J. Kim et al., Carbohydr. Polym. 86 (2) (2011) 903.
[30] Y. Feng et al., Carbohydr. Polym. 87 (1) (2012) 644.
[31] Y. Li et al., NPG Asia Mater. 7 (1) (2015).
[32] R. Xiong et al., Adv. Mater. 28 (7) (2016) 1501.
[33] Z. Weng et al., Adv. Energy Mater. 1 (5) (2011) 917.
[34] X. Zhang et al., Carbohydr. Polym. 88 (1) (2012) 26.

Supporting Information for

A Printed, Recyclable, Ultra-Strong and Ultra-Tough Graphite Structural Material

Yubing Zhou[1,†], Chaoji Chen[1,†], Shuze Zhu[2,†], Chao Sui[3], Chao Wang[3], Yudi Kuang[1], Upamanyu Ray[2], Dapeng Liu[1], Alexandra Brozena[1], Ulrich H. Leiste[4], Nelson Quispe[2], Hua Guo[3], Azhar Vellore[5], Hugh A. Bruck[2], Ashlie Martini[5], Bob Foster[6], Jun Lou[3], Teng Li[2,*], and Liangbing Hu[1,*]

[1]Department of Materials Science and Engineering, University of Maryland, College Park, MD 20742.

[2]Department of Mechanical Engineering, University of Maryland, College Park, MD 20742.

[3] Department of Materials Science and Nano Engineering, Rice University, Houston, TX 77005.

[4] Department of Aerospace Engineering, University of Maryland, College Park, MD 20742.

[5] Department of Mechanical Engineering, University of California Merced, Merced, California, 95343.

[6] Trinity Industries, Inc., Dallas, Texas, 75207.

Email: binghu@umd.edu; lit@umd.edu

†These authors contributed equally to this work.

Methods

Mechanical modeling

The full atomistic simulations use the ReaxFF potential (1) as implemented in the Large-scale Atomic/Molecular Massively Parallel Simulator (LAMMPS) simulation package (2). We investigated the effect of the graphite hydrophobic surface in maintaining an in-plane hydrogen bonding network (Fig. S15), and the role of NFC matrix in load transfer in the graphite-NFC composite (Fig. 4a-f). The graphite stack model is shown in Fig. 4c,f. The edges of graphite stack are terminated with hydrogen or hydroxyl groups. For simplicity, the carboxyl groups are not modeled as they are playing a similar hydrogen bonding role as hydroxyl groups. The graphite-NFC hybrid model is built according to an approximate mass ratio of 50% of graphite over the total mass. Initially a very large periodical simulation box was created, which could host spatially-separated 10 NFC chains and one graphite stack. The entire system was then equilibrated at statistical ensemble at 300 K and 1 atm pressure, using the Nosé−Hoover thermostat and barostat. During this equilibration process, the periodical simulation box shrinks, mimicking the experimental synthesis process, which gives rise to the graphite-NFC hybrid structure model (Fig. 4a,d). The construction of the pure NFC structure model (or the pure graphite structure model) is similar but without the filling of the graphite stack (or the NFC chains) (Fig. 4b,e). The mechanical deformation is then enforced on the periodical simulation box. Deformation is applied in which one dimension of the simulation box is incremented at each step of the simulation to produce a constant engineering tensile strain rate of 5×10^{8} s^{-1}. Engineering stress-strain curves are reported, where the normal stress component of the simulation box along the loading direction is reported as stress. Time averages of stress were taken at frequent time intervals during the entire simulation. In the graphite-NFC hybrid structure case, the stress contribution from its graphite constituent is assessed by adding up the atomic stress values of the atoms that belong to graphite only.

The underlying strengthening and toughening mechanisms of the graphite-NFC composite can be revealed via these molecular dynamics simulations. It is shown that graphite flakes play a pivotal role in the high strength and toughness of the graphite-NFC composite. The introduction of such a non-hydrogen bonding surface into the hydrogen-bonding-rich NFC matrix causes disruption of the hydrogen bonding network among the NFCs. As a result, the hydrogen bonds are re-oriented tangentially to the graphite surface to minimize disruption of the hydrogen bonded 3D network of the NFCs (Fig. S15). In other words, the hydrogen bonding density of the NFC matrix, projected along the tensile loading direction (i.e., tangential to the graphite surface), increases substantially compared with that without graphite surfaces. Furthermore, the edges of the natural graphite flakes are terminated with hydrogen atoms as well as a few hydroxyl and carboxyl groups (Fig. 4c,f). In a hydrogen-bonding-rich NFC matrix, the spatial gaps between the edges of the graphite flakes can be filled by flexible NFCs during the fabrication process of the graphite-NFC hybrid film (Fig. 4a,d). Due to the high density of hydrogen-bonding sites provided by the gap-filling NFCs, most of the sparse-distributed hydroxy groups at the edges of the graphite flakes are able to form hydrogen-bonds with the NFC matrix. As a result, a large amount of interfaces between graphite flake edges and NFC matrix are contributing to the load transferring through hydrogen bonding. Therefore the load transferring capacity of the NFC matrix increases in the presence of graphite hydrophobic surfaces, and the load transferring capacity of graphite flakes increases in the presence of the NFC matrix, showing a strong

synergistic effect. In contrast, for the graphite flakes in a pure graphite film, such a mechanism is quite limited in effect because of the sparse distribution of hydrogen-bonding sites at the edges, as well as large distribution of spatial gaps between the edges (Fig. 4a-f). Therefore, the pure graphite film can barely sustain larger deformation and the ductility is low, as the van der Waals bonds and the few hydrogen bonds are fractured at small strain. As shown in Fig. 4h, the pure graphite structure fractures at a much lower strain than that of the graphite-NFC hybrid structure and pure NFC structure, the latter two featuring an extensive hydrogen bonding network provided by the NFC matrix. In addition, the massive and stable hydrogen bonding network between the NFC matrix and graphite flakes allows the entire system to sustain much larger deformation, as evidenced by the finite stress contribution from the graphite stacks in the hybrid model, beyond the fracture strain of which the pure graphite film fails (Fig. 4h).

The mechanism obtained from molecular dynamics simualtions also suggests that there should exist an optimized ratio between the filling of graphite stacks and NFC chains. In practice, on one hand, adding too much graphite is not always beneficial, as the connection between the graphite stacks could be compromised due to the shortage of supply of NFC chains. On the other hand, adding too many NFC chains may also not always be beneficial. In the limiting case, such a scenario reduces back to a pure NFC film. The mechanism obtained from the molecular dynamics simulations can further explain Fig. 3b, as the pure graphite film fractures much easier than the graphite-NFC hybrid film and pure NFC film, the latter two featuring an extensive hydrogen bonding network provided by the NFC matrix.

Experimental setup and details of pulling graphite flakes from the NFC matrix

We employed an in-house nanomechanical tester to pull out multi-layer graphite flakes. The nanomechanical tester was assembled with two independent linear stages (Newport Corporation, CA, USA), four pico-motors (Newport Corporation, CA, USA), and an AFM probe (Bruker AFM Probes, CA, USA). This tester can achieve 3D nanomanipulation, and the displacement resolution (d_0) is ~30 nm. The spring constant k of the AFM probe was 0.16 N/m, therefore the force resolution (F_0) is calculated to be 4.8 nN according to $F_0 = k \times d_0$. We chose a flat AFM probe, at the end of which there was no cone-shaped tip, so that the edge of the graphite flakes can be completely attached to the AFM probe for better sample alignment.

The samples with fracture section were first fixed on a metal block using silver glue, which was then installed in the chamber of an SEM along with the nanomechanical tester. We note that the cantilever of the AFM probe needs to be parallel to the fracture surfaces of the samples to ensure that there is uniaxial loading on the graphite flakes. The end of the AFM probe was covered by a thin layer of SEM-compatible glue, which enabled the AFM probe to be attached to the edge of a single graphite flake by careful nanomanipulation. Lastly, the contact region between the graphite flake and the AFM probe was exposed to electron beam radiation for about 20 s, so that the graphite flake would be strongly bound to the AFM probe. Then the probe was gradually moved away from the fracture surface of the sample with a constant rate of 30 nm/s, until a potential failure occurred.

As shown in Fig. 5e-g, at first with the increase of the pulling force (F_p), there was no obvious change in the area (S) of the graphite flake exposed to the field of vision, indicating good interface bonding between the graphite flake and matrix during this stage. When F_p reached a maximum value of F_{max} = 3.39 μN, the partial graphite flake was pulled out from the matrix,

leading to an obvious increase of S from 11.53 to 18.42 μm^2, with a consequent change of morphology (Fig. 5h). After that, a debonding failure occurred between the graphite flake and the AFM probe (Fig. 5g). This debonding failure indicated that only part of the graphite flake was pulled out and another part remained in the matrix. A possible reason is that due to the irregular shape of the graphite flake embedded in the matrix, and the fact that there is a strong interlocking effect between the graphite flake edge and matrix, it therefore requires a larger F_p to sustain a complete pullout. Based on the pulled out section of the graphite flake from the matrix, the interfacial shear strength (τ) was estimated to be 0.28 MPa according to $\tau = F_{max}/2S_p = F_{max}/2(S_1-S_0)$, in which S_p is the pullout area from the matrix, and S_0 and S_1 are the areas exposed to the field of vision before and after the test. It was noted that for fracture sample #3 (Fig. S17d-g), because the thickness of the fracture part on the AFM probe was very thin, it rapidly rolled up and attached to the AFM probe upon the electron beam effect. This is why we did not observe the suspended fractured component.

We can determine a full fracture from two aspects. One is that the area sum of the two parts of the fractured graphite flake after the test is approximately equal to the area of the graphite flake before the test. Another one is that the crack morphologies of two fractured parts coincide (Fig. S17a-c). Accordingly, the partial fracture can also be determined by two structural features. On the one hand, we can observe that whether part of the fractured graphite flake remains on the AFM probe. This is easy to identify by comparing the images before and after the test. On the other hand, there is almost no change in the morphology of the graphite flakes exposed to the field of visional before and after the test (Fig. 4a-h, Fig. S18d-k).

References

1. Mattsson, T. R.*, et al.*, *Physical Review B* (2010) **81** (5), 054103.
2. Plimpton, S., *Journal of computational physics* (1995) **117** (1), 1.

Supplementary Figures

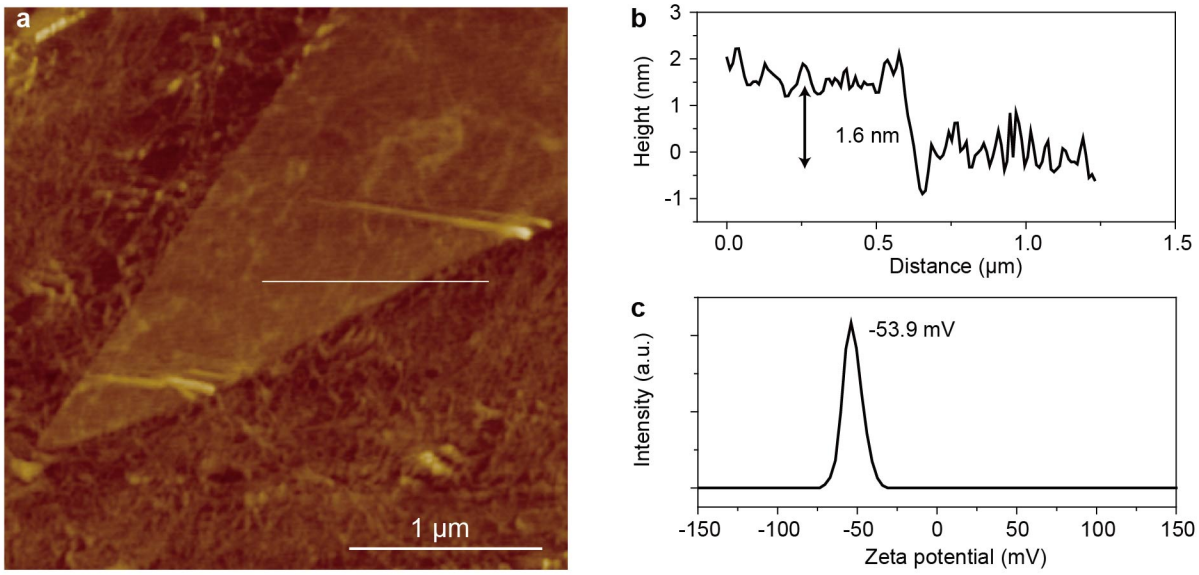

Figure S1. (a) AFM images of the graphite-NFC solution. (b) Height distribution along the line in (a). (c) Zeta potential of the graphite-NFC solution.

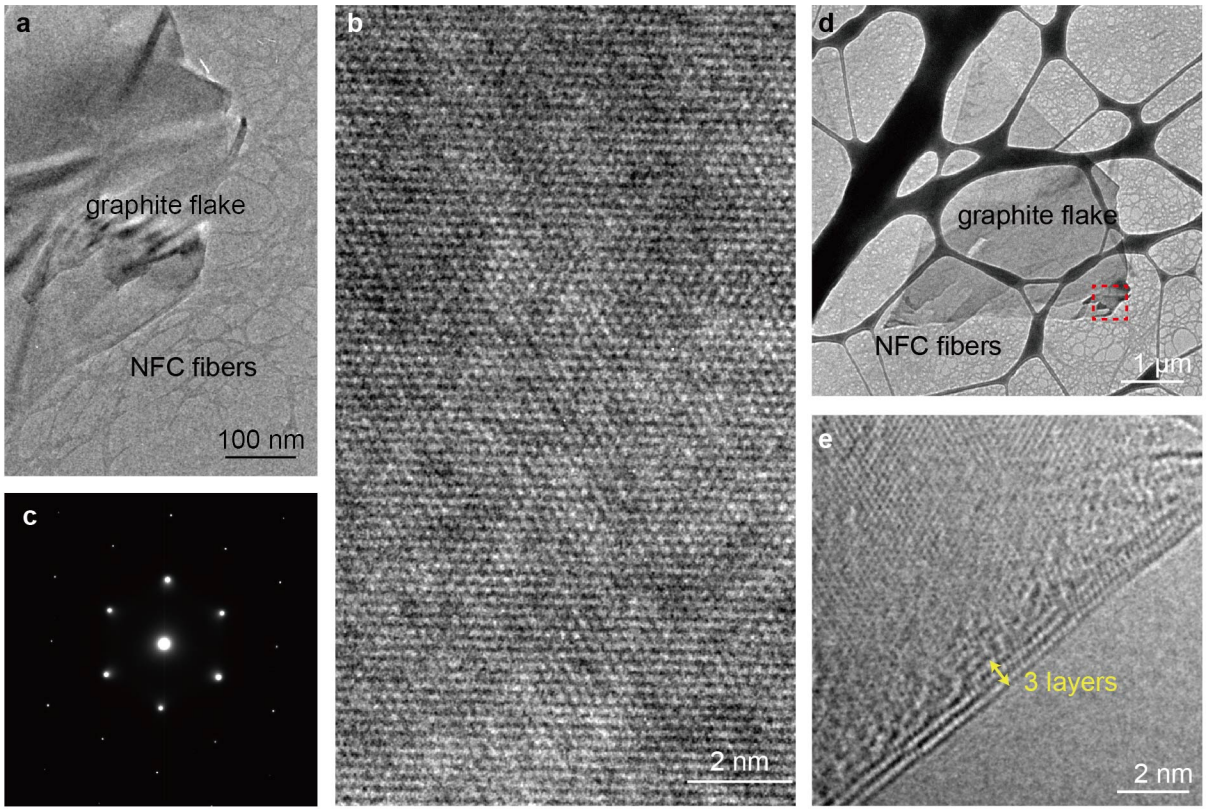

Figure S2. (a-c) Low magnification TEM (a), the corresponding high resolution TEM image (b), and an SAED pattern (c) recorded from the same piece of graphite demonstrate that the ultrathin nanoflake is structurally uniform and highly crystalline, indicating the sonication process introduces few defects. (d,e) Low-magnification TEM (d) and the corresponding high resolution TEM image (e) of the folded edge of the graphite flake, in which the layered structure of the graphite, with alternating bright and dark fringes, is clearly visible. The periodic spacing of these fringes is ~0.34 nm, corresponding to the periodicity of graphite.

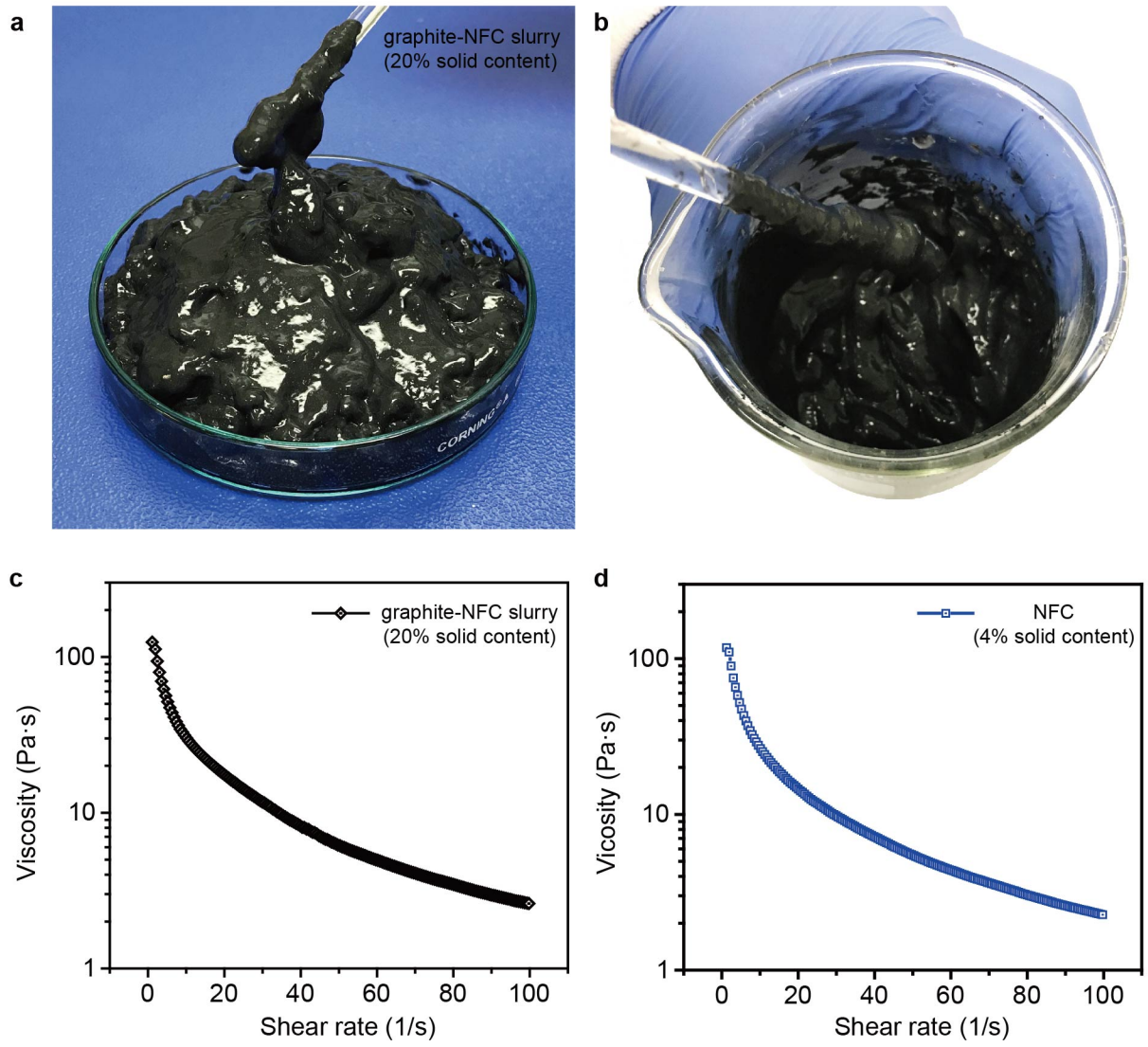

Figure S3. (a,b) Photos of the 20 wt% graphite-NFC slurry. (c,d) Rheological properties of the graphite-NFC (c) and NFC (d) slurries. With almost the same shear viscosity, the graphite-NFC slurry exhibits a significantly higher solid content than the NFC slurry.

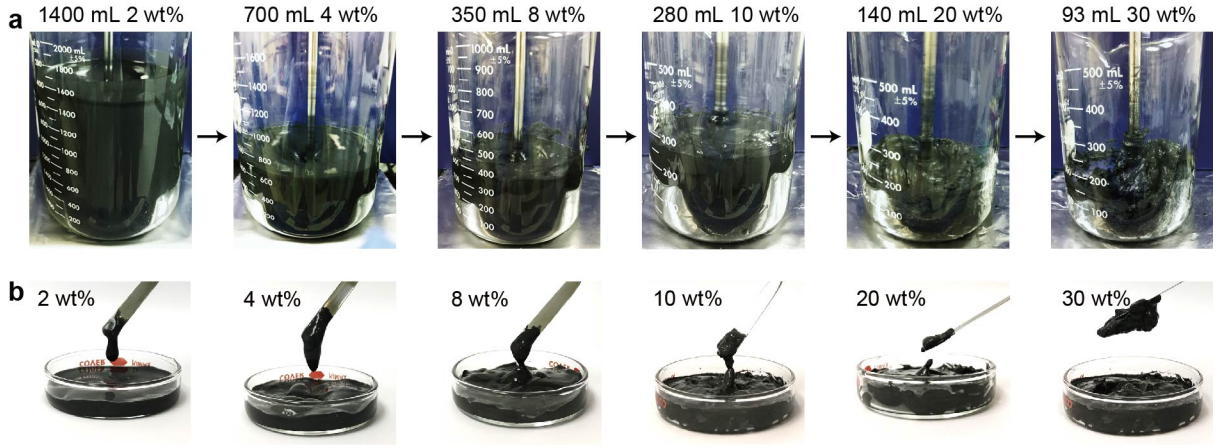

Figure S4. (a) The initial graphite-NFC slurry with 2 wt% solid content was put on a heating stage at 110 ºC. High speed stirring was also employed to ensure the uniformity of the whole slurry system. The solid content can double when halving the volume. (b) The solution behavior of graphite-NFC slurries is strongly dependent on the solid content. 30 wt% slurry behaves like an elastic gel, while the dilute sample (2 wt%) exhibits a fluid-like behavior.

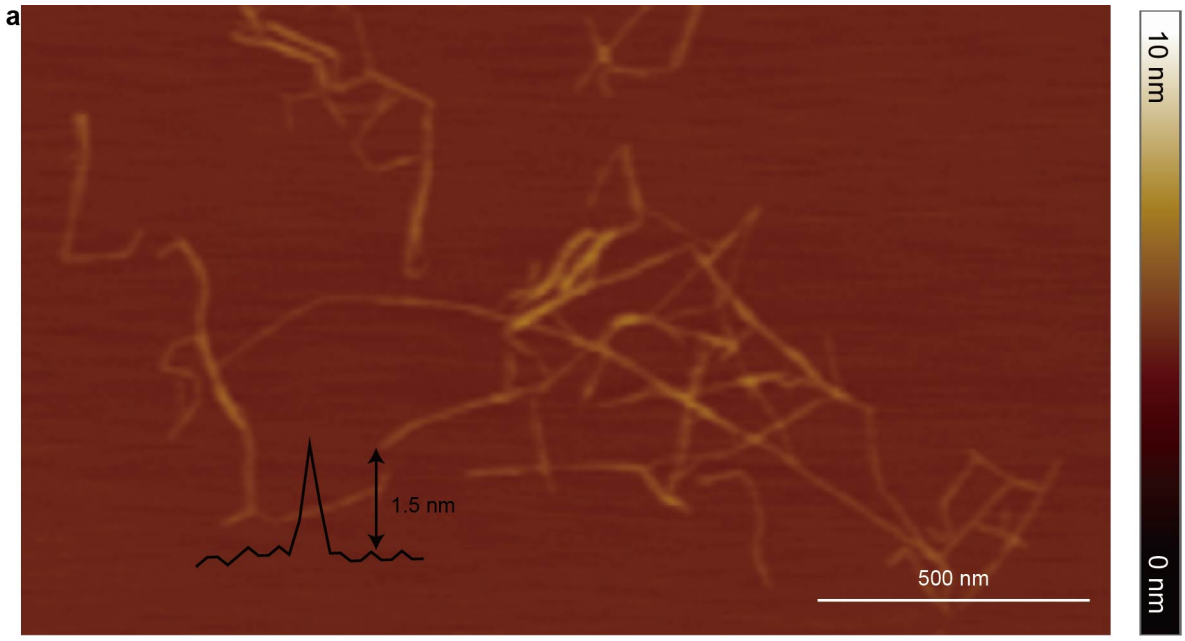
a
10 nm
0 nm
1.5 nm
500 nm

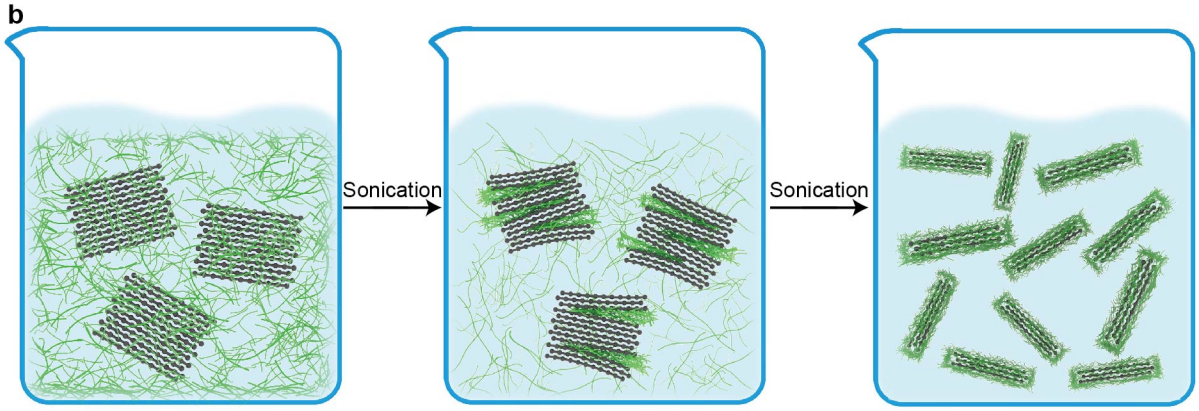
b
Sonication
Sonication

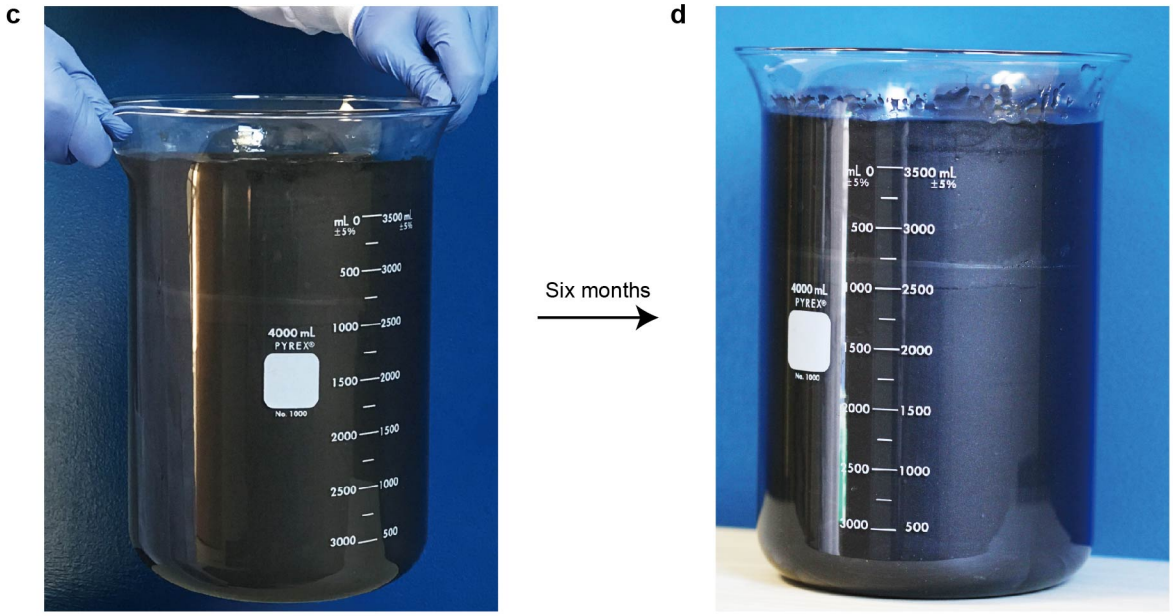
c
d
Six months
4000 mL
PYREX®
No. 1000

Figure S5. (a) AFM image of NFC fibers with mean diameters of 2 nm. (b) Graphite was dispersed in NFC solution and exfoliated into few-layer graphite flakes by sonication. (c) A 4 L solution of the graphite-NFC slurry with 20 wt% solid content, (d) which remains stable after six months refrigerated storage.

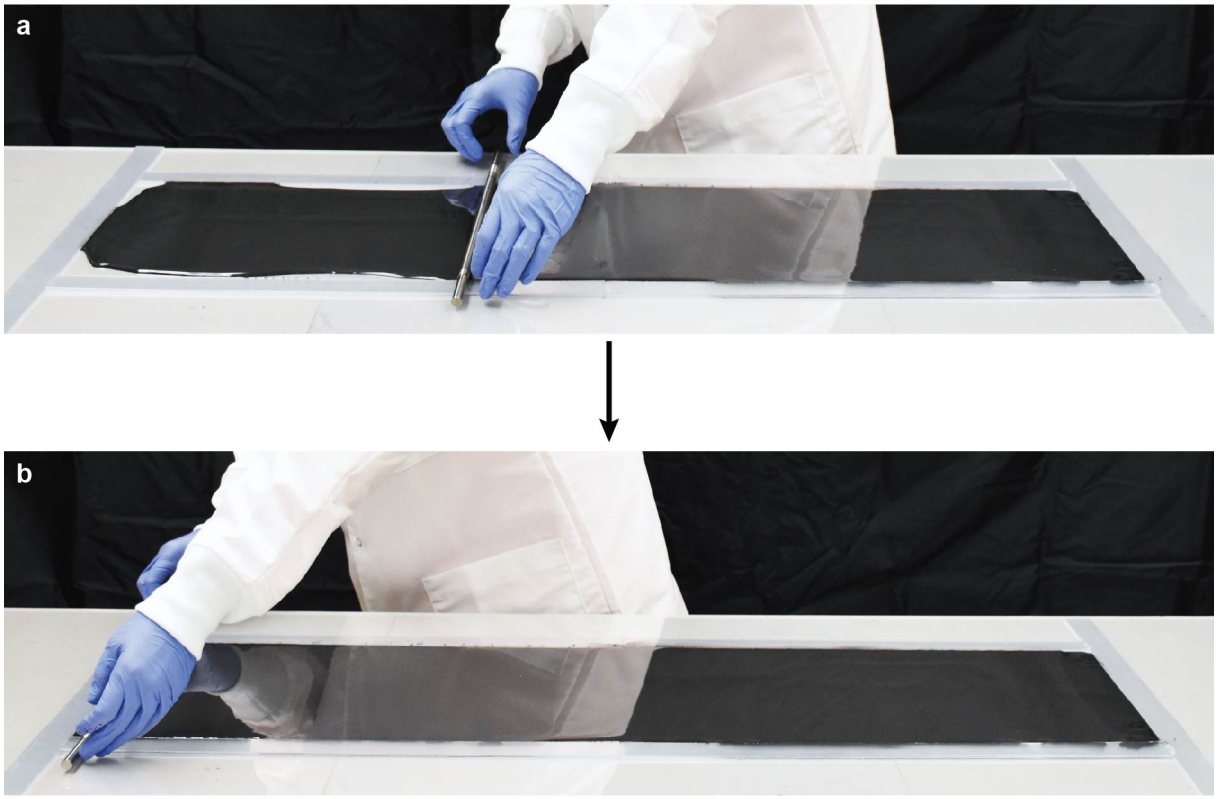

Figure S6. (a,b) The high concentration of 20 wt% solid content graphite-NFC slurry can be uniformly spread using a mayer rod.

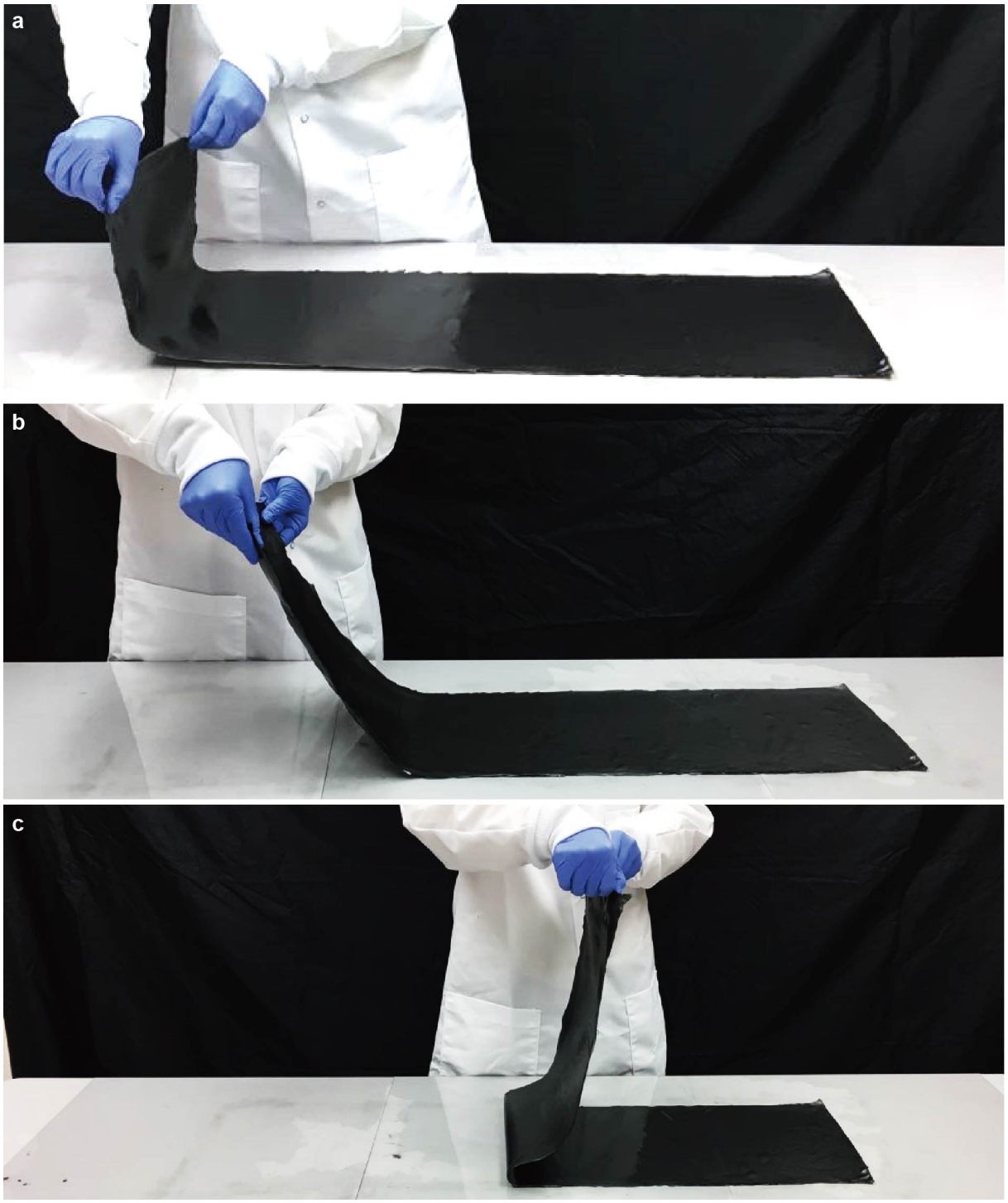

Figure S7. (a-c) After water evaporation, the graphite-NFC composite can be easily peeled off from the substrate. The drying time of the graphite-NFC composites is 48 h.

Figure S8. The graphite-NFC film can retain its morphology before and after bending, springing back on its own.

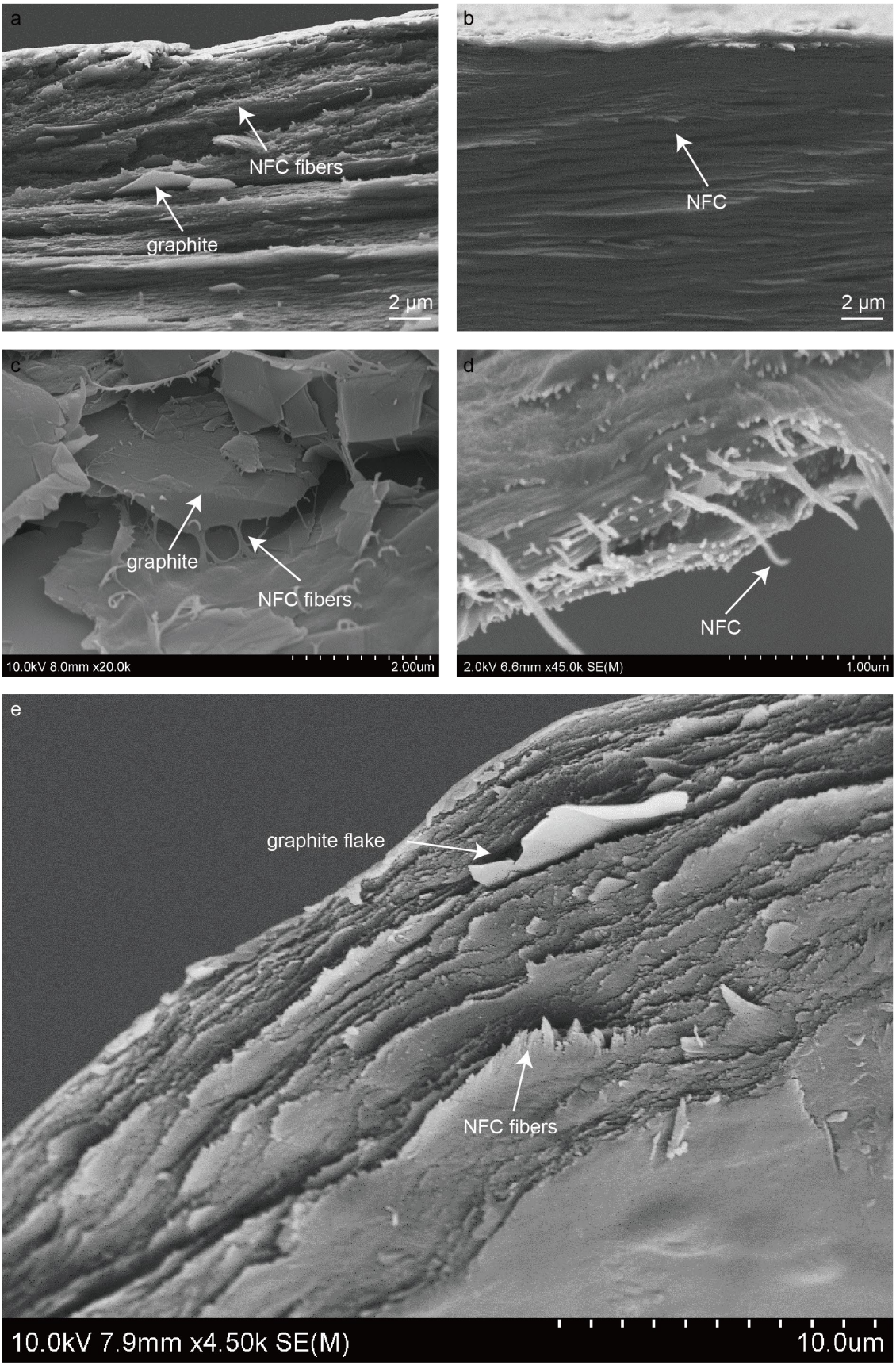
a
NFC fibers
graphite
2 µm
b
NFC
2 µm
c
graphite
NFC fibers
10.0kV 8.0mm x20.0k
2.00um
d
NFC
2.0kV 6.6mm x45.0k SE(M)
1.00um
e
graphite flake
NFC fibers
10.0kV 7.9mm x4.50k SE(M)
10.0um

Figure S9. (a,c) A cross-sectional image of a graphite-NFC composite containing 50 wt% graphite, wherein platelets of multilayered graphite are observed as well as NFC fibers. (b,d) The cross-section of pure NFC nanopaper reveals the homogeneous structure of the NFC fibers. (e) SEM image of the fracture surface by tearing the graphite-NFC composite. The layered structure formed by the few-layer graphite flakes and NFC is clearly observed.

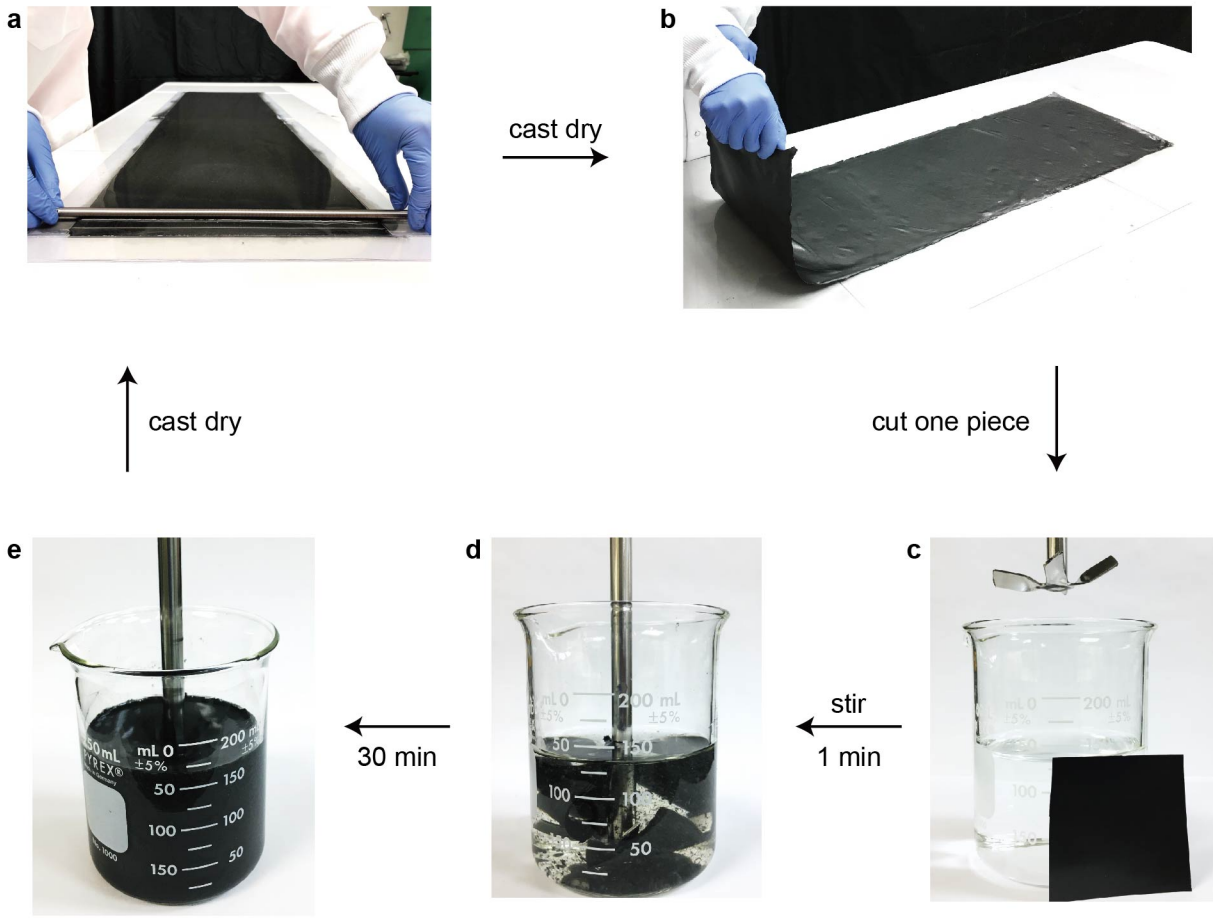

Figure S10. (a) The printing process of the graphite-NFC slurry. (b) The graphite-NFC composite after drying. (c) One piece of the graphite-NFC composite was cut into 5 cm × 5 cm in size and immersed in water, then (d) stirred for one minute, causing the composite to begin to redisperse. The stirring rate was 1000 rpm. (e) After stirring for 30 min, the graphite-NFC composite in water reconstructs a uniform slurry.

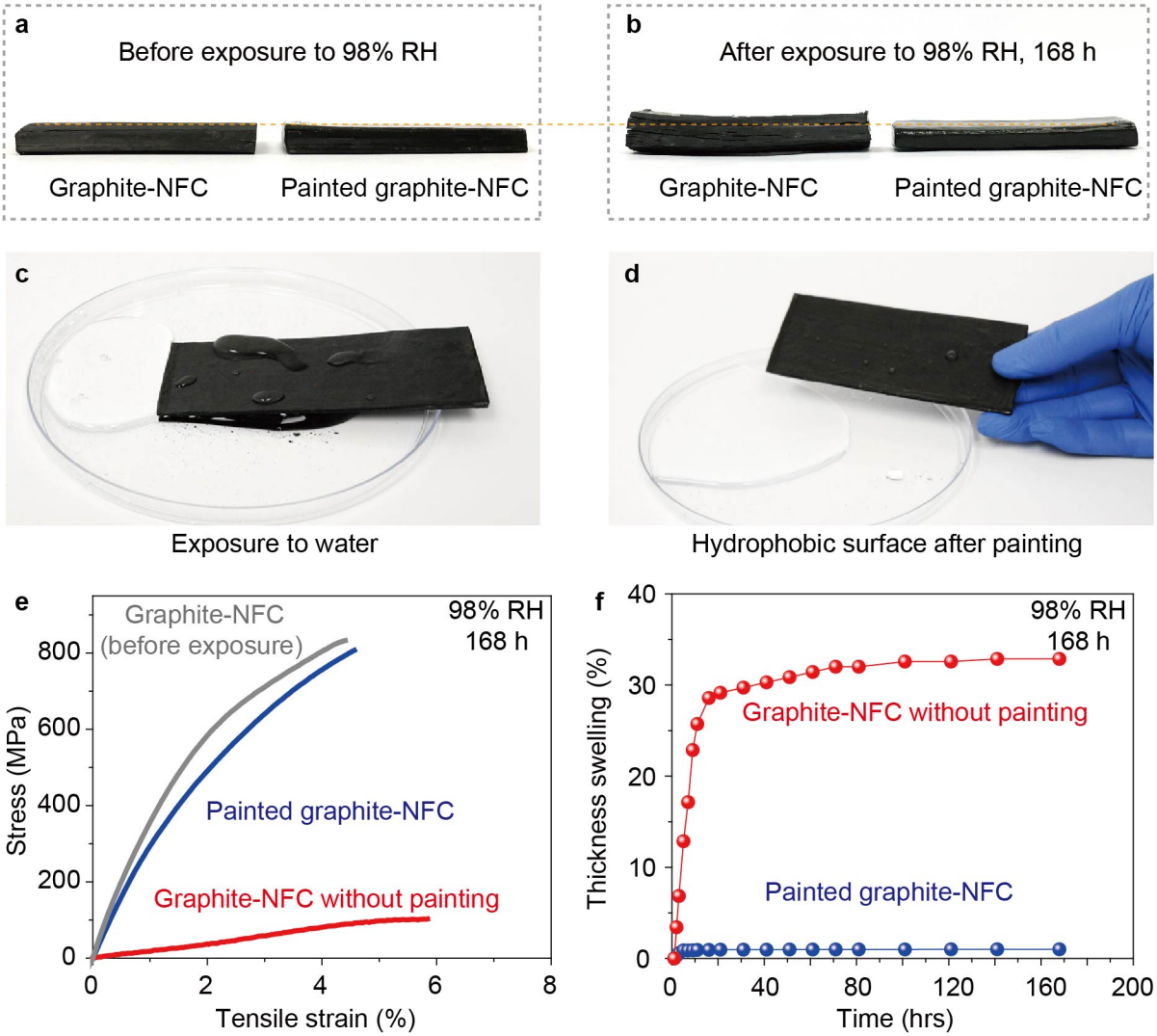

Figure S11. (a,b) Photographs of the graphite-NFC and surface-painted with polyurethane graphite-NFC before (a) and after (b) sustaining 98% RH for 168 h. (c,d) Photographs of the surface-painted laminated thick graphite-NFC plate, which demonstrates high water resistance. (e) Tensile stress-strain curves of the graphite-NFC plate before exposure to humidity and the two graphite-NFC samples after sustaining 98% RH for 168 h. (f) Change in thickness of the two graphite-NFC samples over time at 98% RH.

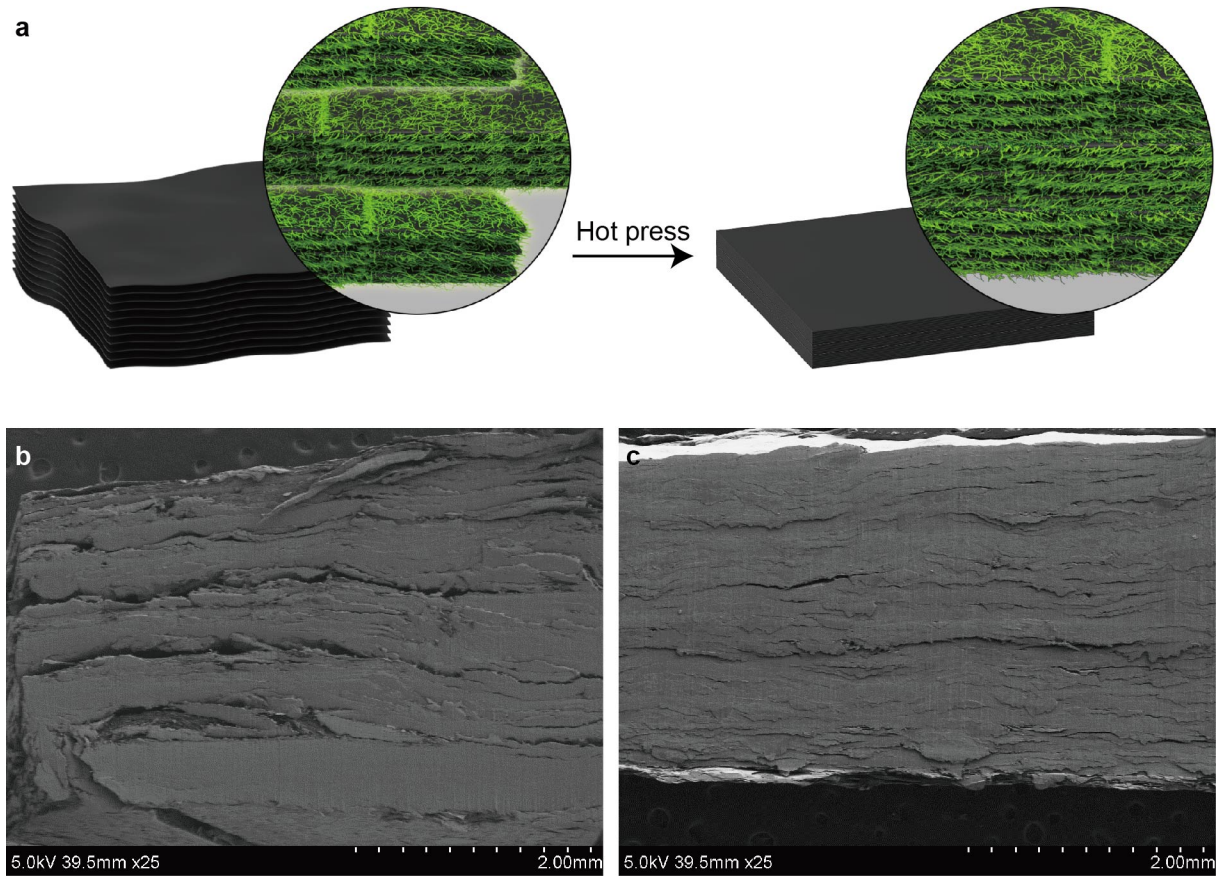

Figure S12. (a) A graphical illustration of the integration of several graphite-NFC composite sheets into a 3 mm thick graphite-NFC block via hot pressing. (b,c) SEM images of the resulting graphite-NFC plate (b) before and (c) after hot pressing. The layers adhere to each other via hydrogen bonding. Each layer cannot be distinguished clearly in the SEM image.

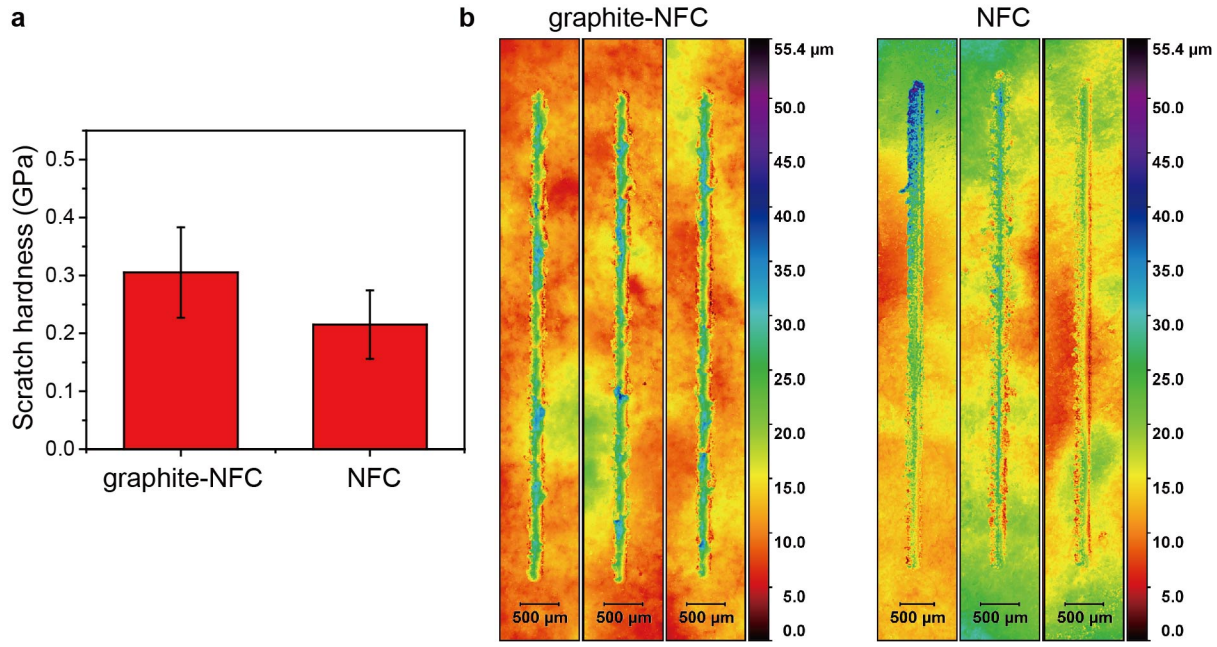

Figure S13. (a) The scratch hardness of the block graphite-NFC and NFC material obtained by hot pressing. (b) Interferometer images of representative scratches on the graphite-NFC composite and NFC nanopaper showing the decrease of the scratch depth of the graphite-NFC composite due to the enhanced hardness.

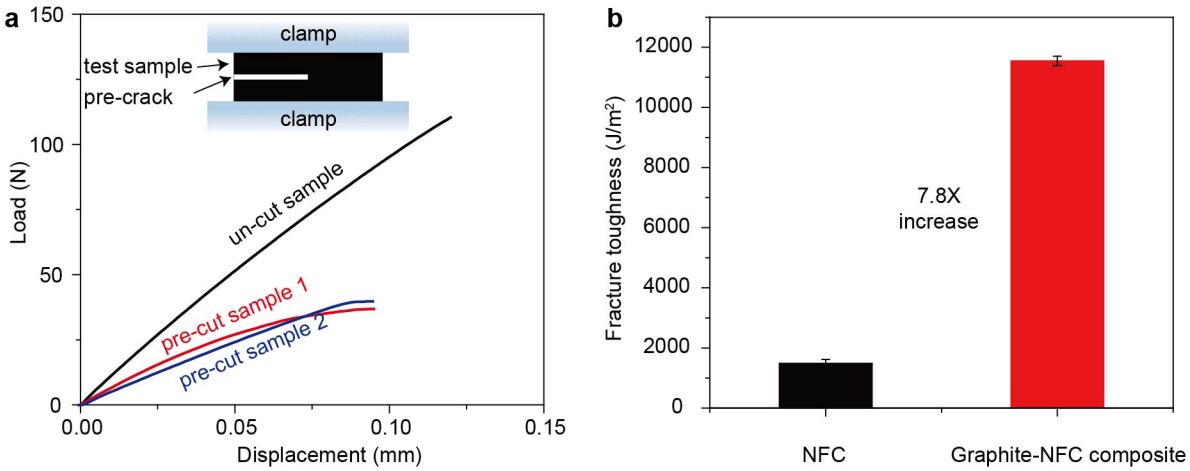

Figure S14. (a) Load displacement curves of the graphite-NFC composite in the fracture toughness test. (b) Fracture toughness of the graphite-NFC composite and NFC nanopaper. The fracture toughness of the NFC nanopaper is adapted from reference (8). We determined the fracture toughness of the graphite-NFC composite using a method introduced in the literature (8), in which a precrack is made along the mid-line between the two clamps.

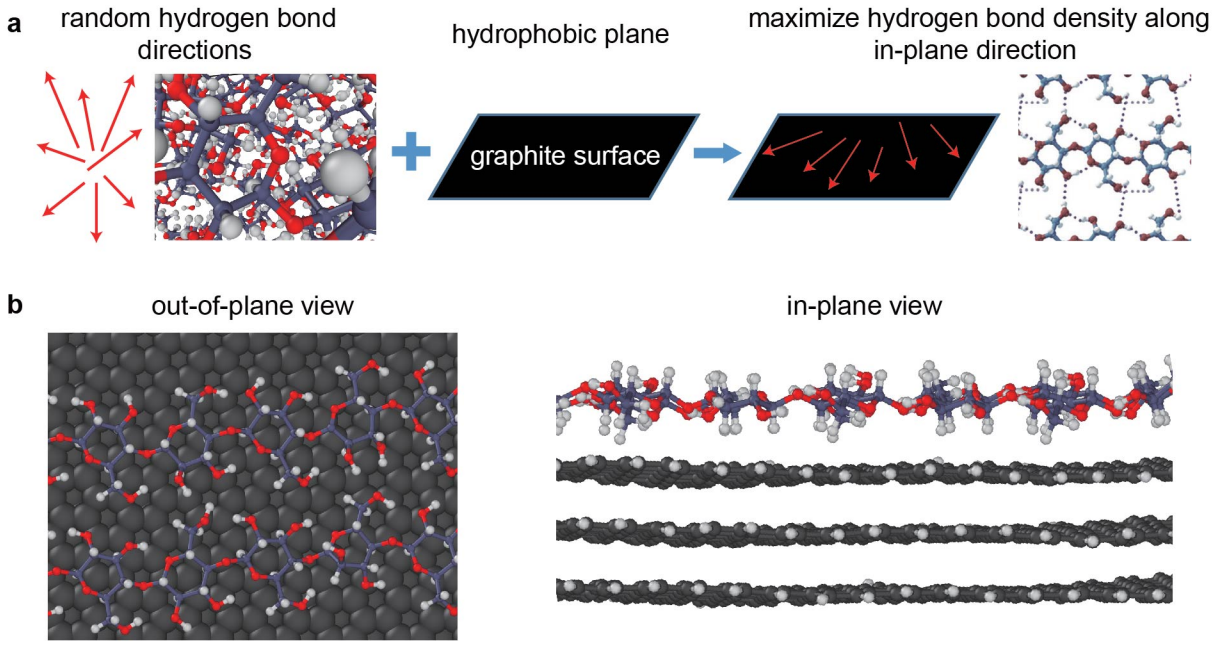

Figure S15. (a) Illustration of the effect of the graphite hydrophobic surface in maximizing hydrogen bond density along the in-plane direction. (b) Illustration of the effect of the graphite hydrophobic surface in maintaining an in-plane hydrogen bonding network, as shown via a molecular dynamics simulation.

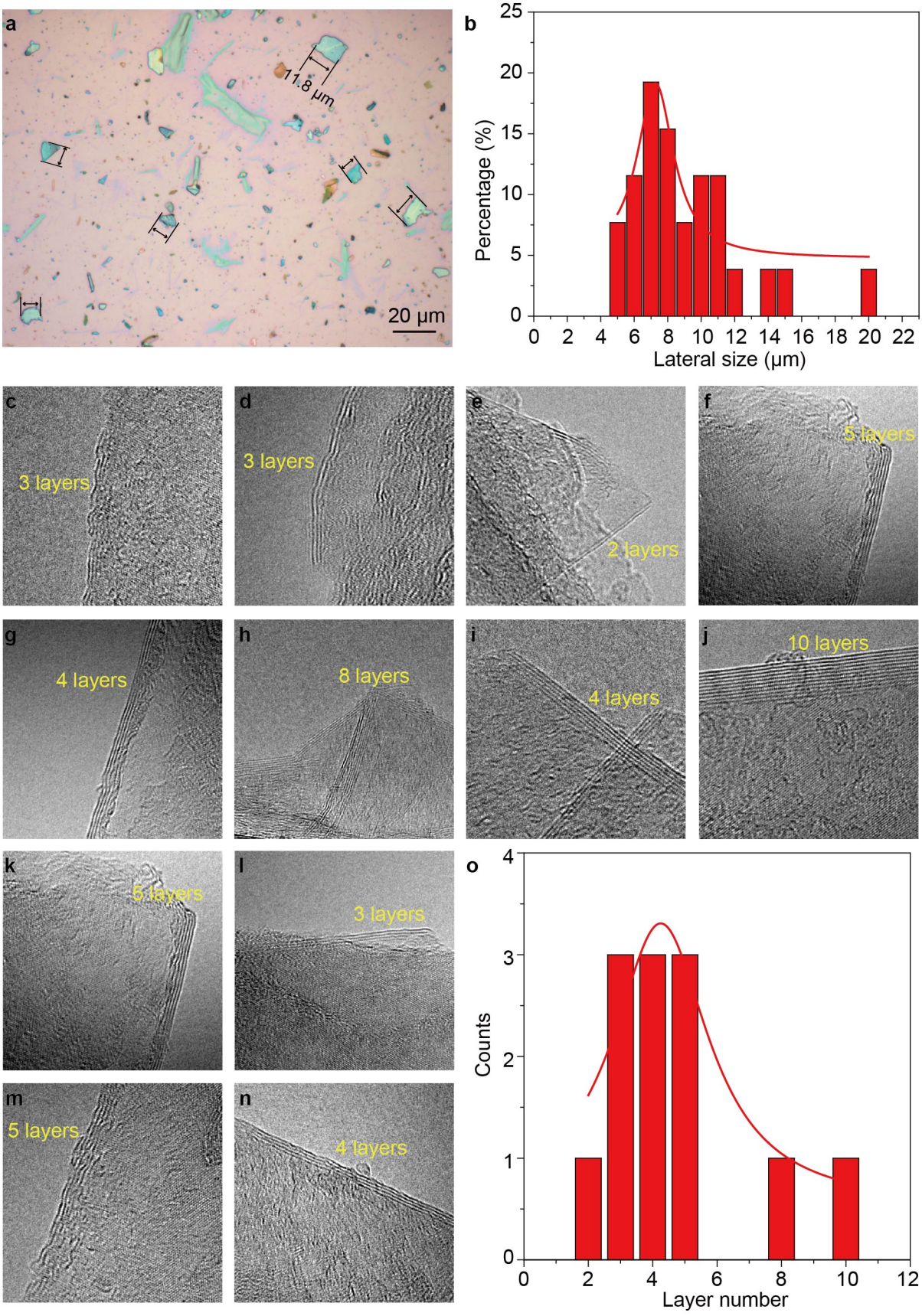
a
11.8 μm
20 μm
b
Percentage (%)
Lateral size (μm)
c
3 layers
d
3 layers
e
2 layers
f
5 layers
g
4 layers
h
8 layers
i
4 layers
j
10 layers
k
5 layers
l
3 layers
m
5 layers
n
4 layers
o
Counts
Layer number

Figure S16. (a) Typical optical image of a diluted graphite-NFC slurry (0.001 wt%) dropped on a SiO_2/Si substrate after drying. The lateral size of individual graphite flakes was determined by the long side. (b) Lateral size distribution histogram for graphite flakes obtained from a substrate area of∼500 μm × 500 μm. (c-n) High resolution TEM images of the folded edges of the graphite flakes. The layered structures with periodical fringes indicate the layer number. (o) Layer number distribution histogram for graphite flakes in (c-n).

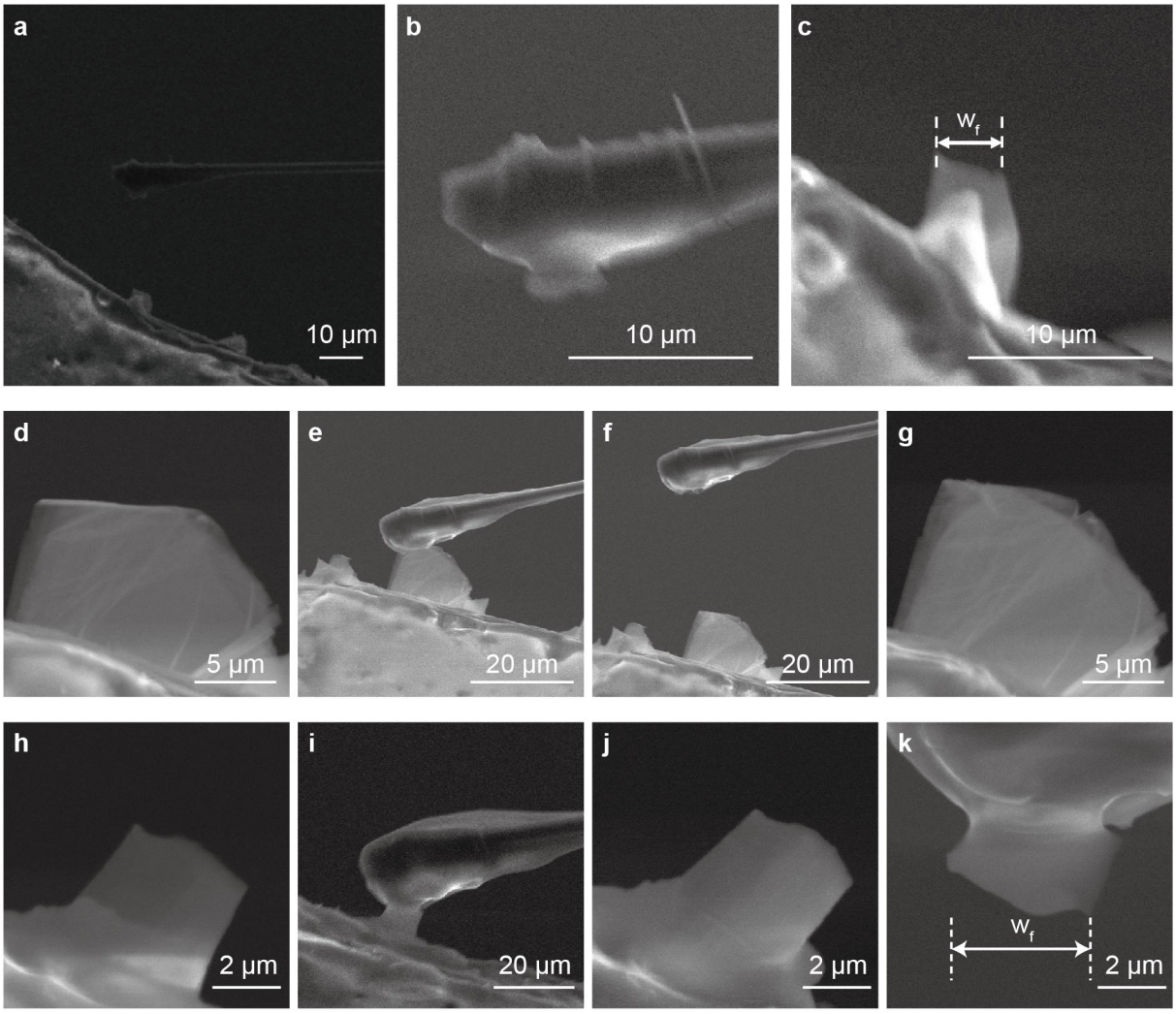

Figure S17. Fracture failure samples: #2 (a-c) Full fracture with the crack morphologies of the two fractured parts coinciding. #3 (d-g) and #4 (h-k) demonstrate the partial fracture of graphite flakes, because of no change in the morphology of the graphite flakes exposed to the field of vision before and after the test.

Table S1. Comparison of the structural and mechanical properties of graphite-NFC composite and other reported graphene/cellulose composites.

Material	2D component	Flake size	Solid content	Process		Mechanical performance		Manufacturability (demonstrated)			Ref.
				Chemical	Temp (℃)	Strength (MPa)	Toughness (MJ/m^3)	Method	In-plane dimension	Mass (g)	
GO/cellulose composite	GO	<1 μm	0.4 wt%	$NaNO_3$, H_2SO_4, $KMnO_4$, H_2O_2	60	97.8	4.4	Casting	~1 cm× 1 cm	~0.003	Ref.30
BC/GO nanocomposite	GO	<1 μm	2.2 wt%	$NaNO_3$, H_2SO_4, $KMnO_4$, H_2O_2	80	242	~7	Filtration	~4 cm × 4 cm	~0.01	Ref.31
Cellulose/GO composite film	GO	<1 μm	4 wt%	$NaNO_3$, H_2SO_4, $KMnO_4$, H_2O_2	80	83.1	~2	Filtration	~4 cm × 4 cm	~0.1	Ref.17
GO/NFC fibers	GO	<1 μm	1.1 wt%	$NaNO_3$, H_2SO_4, $KMnO_4$, H_2O_2	N/A	442	~5	Wet-spinning	~40 μm × 40 μm	0.015	Ref.32
CNC/graphene membrane	RGO	2-8 μm	0.3 wt%	$NaNO_3$, H_2SO_4, $KMnO_4$, H_2O_2	N/A	655	3.9	Spin assisted layer-by-layer assembly	~1 cm × 1.5 cm	0.04	Ref.33
Graphene/ cellulose paper	RGO	<1 μm	1.4 wt%	$NaNO_3$, H_2SO_4, $KMnO_4$, H_2O_2	70	273	~15	Filtration	~4 cm × 4 cm	~0.03	Ref.18
Graphene/ cellulose paper	RGO	~2 μm	0.02 wt%	$NaNO_3$, H_2SO_4, $KMnO_4$, H_2O_2	80	8.67	~0.13	Filtration	~3.5 cm × 3.5 cm	~0.04	Ref.34
Cellulose/ graphene film	RGO	< 1 μm	<1 wt%	Acids (HNO_3, H_2SO_4, HCl), and $KClO_3$	85	148	~10	Filtration	~4 cm × 4 cm	~0.04	Ref.35
Graphite-NFC composite	**Graphite flakes**	**~11 μm**	**20 wt%**	**Water**	**Room temp.**	**1000**	**30.0**	**Printing**	**120 cm × 30 cm**	**8.64**	**Our work**

Table S2. Geometrical and mechanical parameters and failure modes of the fracture samples. #1 is the sample shown in Figure 4a-d.

Sample	Maximum pulling force F_{max} (μm)	Effective fracture width w_f (μm)	Failure mode
#1	5.13	4.03	Partial fracture
#2	3.88	3.74	Full fracture
#3	3.73	3.85	Partial fracture
#4	4.76	4.02	Partial fracture